A 2 million year hydroclimatic context for hominin evolution in southeastern Africa

Thibaut Caley[1*], Thomas Extier[1,2], James A. Collins[3,4], Enno Schefuß[5], Lydie Dupont[5], Bruno Malaizé[1], Linda Rossignol[1], Antoine Souron[6], Erin L. McClymont[7], Francisco J. Jimenez-Espejo[8], Carmen Garcia-Comas[9], Frederique Eynaud[1], Philippe Martinez[1], Didier M. Roche[2,10], Stephan J. Jorry[11], Karine Charlier[1], Mélanie Wary[1], Pierre-Yves Gourves[1], Isabelle Billy[1], Jacques Giraudeau[1].

1) EPOC, UMR 5805, CNRS, University of Bordeaux, Pessac, France

2) Laboratoire des Sciences du Climat et de l'Environnement, LSCE/IPSL, CEA-CNRS-UVSQ, Université Paris-Saclay, F-91191 Gif-sur-Yvette, France

3) GFZ - German Research Center for Geosciences, Section 5.1 Geomorphology, Organic Surface Geochemistry Lab, D-14473 Potsdam, Germany

4) Alfred Wegener Institute Helmholtz Centre for Polar and Marine Research, Am Alten Hafen 26, D-27568 Bremerhaven, Germany

5) MARUM – Center for Marine Environmental Sciences, University of Bremen, D-28359 Bremen, Germany

6) PACEA, UMR 5199, CNRS, University of Bordeaux, Pessac, France

7) Department of Geography, Durham University, Durham, DH1 3LE, UK

8) Department of Biogeochemistry (JAMSTEC), Yokosuka, Japan

9) Research and Development Center for Global Change, (JAMSTEC), Yokohama, Japan

10) Vrije Universiteit Amsterdam, Faculty of Science, Cluster Earth and Climate, de Boelelaan 1085, 1081HV Amsterdam, The Netherlands

11) Unité Géosciences Marines, Institut Français de Recherche pour l'Exploitation de la Mer (IFREMER), Brest, France

[*]**Corresponding author. Email: *thibaut.caley@u-bordeaux.fr***

Abstract

The past two million years of eastern African climate evolution is poorly constrained despite its assumed role in early human evolution[1-4]. Rare paleoclimate records from northeastern Africa suggest progressively drier conditions[2,5] or a stable hydroclimate[6]. In contrast, the only long records from Lake Malawi in tropical southeastern Africa revealed a trend towards a progressively wetter climate over the last 1.3 Ma[7,8]. The climatic forcings that controlled these past hydrological changes are also a matter of debate. Some studies suggest a dominant local insolation forcing on hydrological changes[9-11] whereas others infer a potential influence of sea surface temperature (SST) changes in the Indian Ocean[8,12,13]. We present a multi-proxy reconstruction of hydrological changes in the Limpopo River catchment of southeastern Africa (20-25°S), in conjunction with a SST reconstruction in the southwestern Indian ocean over the past 2.14 Ma. Here, we show that hydroclimate in the region is controlled by an interplay between low latitude insolation forcing (precession and eccentricity) and high latitude ice volume changes. The long-term aridification in the Limpopo catchment between around 1 Ma and 0.6 Ma is opposite to the hydroclimatic evolution at Lake Malawi and seems related to equatorward contraction of the rainbelt in response to increased ice volume at high latitudes. By impacting local terrestrial ecosystems, the observed hydroclimate changes in southeastern Africa both in terms of long-term state and marked precessional variability could have played a role in early hominin evolution, particularly in the extinction of the species *Paranthropus robustus*.

Subtropical southeastern Africa is a region of critical interest because it bears hominin fossils, enabling a comparison between continental indicators of hominin evolution and nearby marine records of past climate changes. Different modes of climate change have been proposed as major factors influencing hominin speciation, adaptation, or extinction. Some authors stress the impact of long-term trends toward aridity on hominin evolution[1,2] whereas others suggest a crucial role of short periods of extreme climatic variability in driving hominin evolution[3,4].

Paranthropus robustus fossils have been found only in southeastern Africa and exclusively in the Limpopo River catchment (sites of Cooper's D, Drimolen, Swartkrans, Sterkfontein, Kromdraai B and Gondolin) (Fig. 1) from at least ~2 Ma to 0.9 Ma (Extended Data Table 1). It is unclear whether climate stress could have played a role in its extinction.

To investigate the hydroclimatic context of the environment *P. robustus* lived in, we reconstructed Quaternary hydrological cycle changes in subtropical southeastern Africa (20-25°S) to determine the drivers of variability and to identify the long-term climate evolution of this region. We used marine sediment core MD96-2048 (26°10'482''S, 34°01'148''E, 660 m water depth) from offshore the Limpopo River (Fig. 1). The chronology of MD96-2048 is established by tuning the $\delta^{18}O$ benthic foraminifera signal to the reference LR04 stack (Fig. 2) (Methods), confirming that the core covers the last 2.14 Ma. We present a multi-proxy record of hydrological changes in the Limpopo catchment together with a sea surface temperature record of the southwestern Indian Ocean (Fig. 2).

Modern precipitation in the Limpopo catchment is dominated by austral summer rainfall associated with the Intertropical Convergence Zone (ITCZ) extending southwards to 15-20°S (Fig. 1). Changes in the hydrological cycle in the catchment are imprinted on Limpopo river discharge. We observe large changes in terrestrial (Fe) versus marine (Ca) sedimentary

elemental ratios, indicating changes in terrestrial discharge by the Limpopo River, at orbital and longer timescales (Fig. 2, Extended Data Fig. 1). Maxima in ln(Fe/Ca) ratios are associated with a more depleted stable hydrogen isotope composition of plant waxes (δD_{wax}) (Fig. 2), which reflect the isotopic composition of precipitation and are indicative of higher regional rainfall amount[10,12,14] (Extended Data Fig. 2) (Methods). Maxima in ln(Fe/Ca) ratios are also associated with maxima in brGDGT concentrations (commonly found in soils and attributed to Limpopo River runoff[15]) and more enriched plant wax $\delta^{13}C$. A previous study on core MD96-2048 over the last 0.8 Ma interpreted shifts towards more depleted $\delta^{13}C_{wax}$ as potentially reflecting more humid conditions[16]. However, $\delta^{13}C_{wax}$ is a proxy for the contribution of waxes from C_3 versus C_4 plants to the sediments, which can be influenced by many other factors than aridity/humidity. We attribute the enriched plant $\delta^{13}C_{wax}$ at times of depleted δD_{wax} values, increase ln(Fe/Ca) and brGDGT concentration to stronger transport of C_4 plant material from the upper Limpopo catchment in addition to the extension of riverine swamps and floodplains harboring abundant C_4 sedges (Fig. 2, Extended Data Figs. 3 and 4).

The ln(Fe/Ca) ratio has the highest temporal resolution (300 years on average) of the proxies employed here. Statistical analyses indicate significant 19 and 23 kyr cycles (precession) and 100 kyr and 400 kyr cycles (eccentricity) but no significant 41 kyr cycle (obliquity) (Extended Data Figs. 5). The dominance of eccentricity and precession cycles indicates a strong influence of low-latitude insolation on hydrological changes in the Limpopo catchment. Rainfall and precession maxima are in phase (i.e. maxima of local insolation in the southern hemisphere) (Extended Data Figs. 3, 5).

Modern-day rainfall in the subtropical Limpopo region mostly depends on easterly waves and low-pressure cells largely controlling summer rainfall (November to March, 72 % of the rainfall in Pretoria; Extended Data Fig. 2), and on tropical-extratropical cloud bands and associated thunderstorms[17]. The convective rains are usually associated with the ITCZ and warm, humid easterly winds[17]. Numerical model experiments suggest southern summer insolation forcing exerts a strong and positive effect on monsoon rainfall[11,18]. During precession maxima, higher southern hemisphere summer insolation causes higher temperatures and lower surface pressure over the southern hemisphere, in particular over land[11]. The land/ocean temperature contrast results in stronger easterly moisture inflow onto southeastern Africa. Increased rainfall results from increased convection over and increased humidity transport onto southeastern Africa[11]. Because eccentricity modulates precession amplitudes, increased summer insolation associated with eccentricity increases the variability in rainfall and fluvial discharge in the Limpopo catchment (Fig. 3).

In addition to this, it is thought that sea surface temperature anomalies in the Indian Ocean have an influence on summer rainfall in the region[19]. To explore the potential relationship between hydrological cycle changes and oceanic conditions, SSTs in the southwestern Indian Ocean were reconstructed using two different methods (Methods, Extended Data Fig. 6). There is a significant correlation between SST and orbital parameters at the 100 kyr cycle (glacial-interglacial periodicity) and the 41 kyr cycle (obliquity) (Extended Data Fig. 5). The results confirm a previous study revealing the absence of significant precessional variability in the SST record over the last 800 kyr[15]. This suggests that orbital-scale precipitation changes in southeastern Africa are more closely related to the land/ocean temperature contrast than to SST changes.

Superimposed on the orbital-scale changes, our record displays a long-term trend towards more arid conditions in southeastern Africa between ~1 Ma and ~0.6 Ma (Figs. 2, 3b-c). This period corresponds to the Mid-Pleistocene Transition (MPT), which is marked by ice-sheet expansion and global SST decrease[20] (Fig. 2). In terms of hydrological changes, the record from Lake Malawi covering the last 1.3 Ma has been interpreted to show opposite changes to those we observe for the Limpopo catchment. At Lake Malawi, the climate changed from a

predominantly arid environment between 1.3 and ~1 Ma to generally wetter conditions after ~1 Ma[7,8]. This opposing pattern in hydrological changes between the Limpopo catchment and Lake Malawi suggests a gradual contraction of tropical rainfall from the Limpopo catchment towards lower latitudes in response to the ice sheet expansion during the MPT. This rainfall shift could be related to increased Antarctic ice volume during the MPT[21,22].

The long-term trend towards wetter conditions at Lake Malawi has been explained by a progressively less positive Indian Ocean Dipole (IOD) since ~1 Ma. The IOD can enhance or reduce the precessional variability in low-latitude hydroclimate by modifying the Walker circulation over the Indian Ocean with a diverse response in eastern Africa[23]. A progressively less positive IOD would have generated wetter conditions in southern Africa and increased the precession signal. Whilst the precessional signal increased over time at Limpopo, the observed progressive increase in aridity is contrary to what would be expected with IOD forcing alone (Fig. 3).

Based on our new records and comparison with Lake Malawi published records in eastern Africa we propose that low latitude insolation forcing (precession and eccentricity) and high latitude ice volume changes were the main driver of southeastern African hydroclimate over the last 2 Ma with SST forcing playing a secondary role. Results also highlight a large regional variability in southeastern African hydroclimate.

Hydrological cycle changes in southeastern Africa were likely one of the multiple factors influencing the dispersal and evolution of human relatives[2,4]. The more humid conditions observed between ~2 Ma and 1.75 Ma associated with a maximum in eccentricity forcing correspond to several occurrences of *P. robustus* (Fig. 3, Extended Data Table 1). *Paranthropus robustus* is a species that was overall ecologically variable (eurytopic) but multiple lines of evidence suggest that, from its earliest to its last occurrence, it preferred the C_3 wooded or humid components of environments that were otherwise dominated by C_4 dry-adapted plants. This preference for habitats dominated by C_3 plants, either in woodlands or in humid environments, is well corroborated by the data gained from the paleoecological studies of other contemporaneous animals, indicating large quantities of C_4 vegetation available, but always with a more wooded component and a water source available nearby (Fig. 3B, Extended Data Table 2, Methods)[24]. Interestingly, this more humid period between ~2 Ma and 1.75 Ma is also characterized by the presence of *Australopithecus sediba* in the Limpopo catchment (so far known only at the Malapa site)[25]. Multiple lines of evidence similarly suggest the latter lived in a wooded or humid habitat and had a diet dominated by C_3 plants within an otherwise rather open environment dominated by C_4 plants[25].

Our new data raise the possibility that increasing long-term aridity associated to multi-millennial-scale changes after 1 Ma driven by the MPT (Fig. 3b-d) could have diminished the wooded and/or humid component of the habitat preferred by *P. robustus*. This is in accordance with a trend towards more open and drier landscapes at Swartkrans (Fig. 3B, Extended Data Table 2, Methods).

It has been proposed that extinctions of large mammals are mainly caused by abiotic environmental changes[26]. As a speculative but plausible scenario we propose that the geographic ranges of species preferring wooded and humid habitats, including *P. robustus*, would have contracted and expanded following the precessional (~21 kyr) dry and wet cycles. During the multi-millennial dry periods, the range of populations of those species would have contracted and often become fragmented. These isolated populations would have been especially prone to local extinction through lack of sufficient suitable food, water, and shelters, and related increased competition and predation. During multi-millennial wet periods associated with precessional maxima, preferred woodland and humid habitats would have expanded again. The surviving populations would have thrived again and expanded into their previously occupied range, replacing locally extinct populations. The long-term trend to

increased aridity implies that the dry periods became more and more pronounced between 1 Ma and 0.6 Ma (Figs. 3b and 3d), increasing the likelihood for more numerous extinctions of local populations, until the extinction of the last remaining population, and therefore of the species[27]. Given that the C_3 component of the vegetation preferred by *P. robustus* was never dominant in the landscapes, even during humid periods, its populations would have been especially prone to local extinction during dry periods.

Both the long-term aridification state and the extreme precessional hydroclimate variability (Fig. 3) could thus have contributed to the extinction of *P. robustus*.

References:

1. Vrba, E. S. Environment and evolution: alternative causes of the temporal distribution of evolutionary events. *S. Afr. J. Sci.* **81**, 229–236 (1985).
2. deMenocal, P. B. Plio-Pleistocene African climate. *Science* **270**, 53–58 (1995).
3. Potts, R. Environmental hypotheses of hominin evolution. *Yearb. Phys. Anthropol.* **41**, 93–136 (1998).
4. Maslin, M. A. & Trauth, M. H. in *The First Humans: Origin and Early Evolution of the Genus* Homo (eds Grine, F. E., Fleagle, J. G. & Leakey, R. E.) 151–158 (Springer, 2009).
5. Cerling, T. E. *et al.* Woody cover and hominin environments in the past 6 million years. *Nature* **476**, 51–56 (2011).
6. Blumenthal, S. A. *et al.* Aridity and hominin environments. *Proc. Natl Acad. Sci. USA* **114**, 7331–7336 (2017).
7. Lyons, R. P. *et al.* Continuous 1.3-million-year record of East African hydroclimate, and implications for patterns of evolution and biodiversity. *Proc. Natl Acad. Sci. USA* **112**, 15568–15573 (2015).
8. Johnson, T. C. *et al.* A progressively wetter climate in southern East Africa over the past 1.3 million years. *Nature* **537**, 220–224 (2016).
9. Partridge, T. C., deMenocal, P. B., Lorentz, S. A., Paiker, M. J. & Vogel, J. C. Orbital forcing of climate over South Africa: a 200,000-year rainfall record from the Pretoria Saltpan. *Quat. Sci. Rev.* **16**, 1125–1133 (1997).
10. Schefuß, E., Kuhlmann, H., Mollenhauer, G., Prange, M. & Pätzold, J. Forcing of south-east African wet phases during the last 17,000 years. *Nature* **480**, 509–512 (2011).
11. Simon, M. H. *et al.* Eastern South African hydroclimate over the past 270,000 years. *Sci. Rep.* **5**, 18153 (2015).
12. Tierney, J. E. *et al.* Northern hemisphere controls on tropical southeast African climate during the past 60,000 years. *Science* **322**, 252–255 (2008).
13. Dupont, L. M. *et al.* Glacial-interglacial vegetation dynamics in South Eastern Africa coupled to sea surface temperature variations in the Western Indian Ocean. *Clim. Past* **7**, 1209–1224 (2011).
14. Schefuß, E., Schouten, S. & Schneider, R. R. Climatic controls on central African hydrology during the past 20,000 years. *Nature* **437**, 1003–1006 (2005).
15. Caley, T. *et al.* High-latitude obliquity as a dominant forcing in the Agulhas current system. *Clim. Past* **7**, 1285–1296 (2011).
16. Castañeda, I. S. *et al.* Middle to Late Pleistocene vegetation and climate change in subtropical southern East Africa. *Earth Planet. Sci. Lett.* **450**, 306–316 (2016).
17. Tyson, P. D. & Preston-Whyte, R. A. *The Weather and Climate of Southern Africa* (Oxford University Press, 2000).
18. Kutzbach, J. E., Liu, X., Liu, Z. & Chen, G. Simulation of the evolutionary response of global summer monsoons to orbital forcing over the past 280,000 years. *Clim. Dyn.* **30**, 567–579 (2008).
19. Reason, C. J. C. Subtropical Indian Ocean SST dipole events and southern African rainfall. *Geophys. Res. Lett.* **28**, 2225–2227 (2001).
20. McClymont, E. L., Sosdian, S. M., Rosell-Melé, A. & Rosenthal, Y. Pleistocene sea-surface temperature evolution: early cooling, delayed glacial intensification, and implications for the mid-Pleistocene climate transition. *Earth Sci. Rev.* **123**, 173–193 (2013).
21. Elderfield, H. *et al.* Evolution of ocean temperature and ice volume through the mid-Pleistocene climate transition. *Science* **337**, 704–709 (2012).

22. Pollard, D. & DeConto, R. M. Modelling West Antarctic ice sheet growth and collapse through the past five million years. *Nature* **458**, 329–332 (2009).
23. Tierney, J. E., Smerdon, J. E., Anchukaitis, K. J. & Seager, R. Multidecadal variability in East African hydroclimate controlled by the Indian Ocean. *Nature* **493**, 389–392 (2013).
24. Balter, V., Braga, J., Télouk, P. & Thackeray, J. F. Evidence for dietary change but not landscape use in South African early hominins. *Nature* **489**, 558–560 (2012).
25. Henry, A. G. *et al.* The diet of *Australopithecus sediba*. *Nature* **487**, 90–93 (2012).
26. Žliobaitė, I., Fortelius, M., & Stenseth, N. C. Reconciling taxon senescence with the Red Queen's hypothesis. *Nature* **552**, 92–95 (2017).
27. Foley, R. in *African Biogeography, Climate Change, and Human Evolution* (eds Bromage, T.G. & Schrenk, F.) 328–348 (Oxford University Press, 1999).
28. Xie, P. & Arkin, P. A. Global precipitation: a 17-year monthly analysis based on gauge observations, satellite estimates and numerical model outputs. *Bull. Am. Meteorol. Soc.* **78**, 2539–2558 (1997).
29. Locarnini, R. A. *et al. World Ocean Atlas 2009. Volume 1: Temperature*. (NOAA Atlas NESDIS 68, U. S. Government Printing Office, 2010).
30. Still, C. J. & Powell, R. L. in *Isoscapes: Understanding Movement, Pattern, and Process on Earth through Isotope Mapping* (eds West, J. B., Bowen, G. J., Dawson, T. E. & Tu, K. P.) 179–194 (Springer, 2010).
31. Laskar, J. *et al.* A long-term numerical solution for the insolation quantities of the Earth. *Astron. Astrophys.* **428**, 261–285 (2004).

Supplementary Information is linked to the online version of the paper at www.nature.com/nature.

Acknowledgements: T.C. is supported by CNRS-INSU. Funding from LEFE-IMAGO CNRS INSU project SeaSalt is acknowledged. T.C. was partly supported by the "Laboratoire d'Excellence" LabexMER (ANR-10-LABX-19) and co-funded by a grant from the French government under the program "Investissements d'Avenir", and by a grant from the Regional Council of Brittany (SAD programme). J.A.C. acknowledges funding from the ERC-project "STEEPClim". E.S. and L.D. acknowledge funding through the DFG-Research Center/Cluster of Excellence "The Ocean in the Earth System" at MARUM – Center for Environmental Sciences. A.S. acknowledges funding through the LaScArBx, a programme supported by the Agence Nationale pour la Recherche (ANR-10-LABX-52). Core MD96-2048 was collected during the MOZAPHARE cruise of the RV Marion Dufresne, supported by the French agencies Ministère de l'Education Nationale de la Recherche et de la Technologie, Centre National de la Recherche Scientifique (CNRS), and Institut Paul Emile Victor (IPEV).

Author contributions: T.C. designed the study. T.C., T.E., M.W., and P-Y.G performed the Mg/Ca measurements. L.R. analysed the foraminifera assemblages and T.C. and F.E. analysed the results and performed the transfer function. T.C., T.E., B.M. and K.C performed the $\delta^{18}O$ analyses on foraminifera. T.C., J.G., P.M. and I.B performed the XRF measurements and F.J.J-E and C.G-C. conducted the statistical analyses on XRF. J.A.C. and E.S. performed plant-wax δD and $\delta^{13}C$ analyses. L.D. performed the pollen analysis. A.S. and T.C. produced the synthesis on the ecology and environments of South African hominins and conducted the comparisons to the marine record. T.C. and D.M.R. performed and analysed the iLOVECLIM model results. T.C. analysed the results and all authors participated in the interpretation. T.C. wrote the manuscript with contributions from all authors.

Author Information: Reprints and permissions information is available at www.nature.com/reprints. The authors declare no competing financial interests. Correspondence and requests for materials should be addressed to T.C.

Figure legends

Figure 1: Modern climatology over southern Africa and vegetation types in the Limpopo catchment. a) Averaged precipitation rates for January[28] and annual SST over the Indian Ocean[29]. Black arrows represent the atmospheric circulation over southern Africa during austral summer. The Intertropical Convergence Zone (ITCZ) and the Congo Air Boundary (CAB) are indicated. b) Modelled relative C_4 plant abundance in the Limpopo catchment[30] with indications of topography and bathymetry. Location of core MD96-2048, the Lake Malawi records, the main sites of hominin finds for *Paranthropus robustus* (sites of Cooper's D, Drimolen, Swartkrans, Sterkfontein, Kromdraai B and Gondolin) and *Australopithecus sediba* (Malapa) (Extended Data Table 1) and the Pretoria GNIP station are indicated.

Figure 2: Hydrological changes in the Limpopo catchment compared to sea surface temperatures of the southwestern Indian Ocean over the last 2.14 Ma. a) δD of the *n*-C_{31} alkane of plant waxes. Mean analytical uncertainty of 3 ‰ is indicated. b) $\delta^{13}C$ of the *n*-C_{31} alkane of plant waxes (from Castaneda et al.[16] in light green and this study in dark green). Mean analytical uncertainties of 0.2 ‰ and 0.4 ‰[16] are indicated. c) Pollen percentages of Cyperaceae (data of the last 342 kyr from Dupont et al.[13]). Error bars represent 95 % confidence intervals. d) ln(Fe/Ca) XRF ratios. Arrow indicates the long-term trend discussed in the text. Grey frames represent events of hydrological cycle intensification. e) Principal component of the SST records (Methods). f) $\delta^{18}O$ of benthic foraminifera compared to the reference LR04 curve (data of the last 790 kyr from Caley et al.[15]) (Methods). The Mid Pleistocene Transition (MPT) period is indicated.

Figure 3: Forcings on the hydrological cycle changes in the Limpopo catchment and relationship with hominin evolution over the last 2.14 Ma. A. a) Eccentricity and precession index[31]. b) ln(Fe/Ca) XRF ratios as a proxy of hydrological changes in the Limpopo catchment. Red curve denotes a polynomial fit (9^{th} degree). The MPT and the associated ice-sheet expansion is indicated (orange shading)[20,21]. Grey shading indicates wetter conditions in the Limpopo catchment associated with higher eccentricity. c) Cusum of ln(Fe/Ca) showing deviation from the mean as indicator of hydrological variability in the Limpopo catchment (Methods) (red curves correspond to dry periods, yellow curves to drying periods, dark blue curves to wet periods and light blue curves to humidification periods). d) Precession component of the ln(Fe/Ca) ratios obtained by Gaussian filtering. e) Estimated ages for the main sites that yielded remains of the hominin *Paranthropus robustus* (Cooper's D, Drimolen, Swartkrans and Gondolin) and *Australopithecus sediba* (Malapa) (Extended Data Table 1). B. Enamel $\delta^{13}C$ (‰ V-PDB) of hominins and contemporaneous herbivores at Swartkrans (Extended Data Table 2). Triangles indicate raw data points. The boxplots correspond to the median (horizontal line), the interquartile range (box), and the full range of data (vertical whiskers). Sample sizes are indicated in parentheses. Dash lines highlight the thresholds used to estimate the percentage of C_3 plants-derived foods in the diets.

Methods:

XRF measurements: Element intensities were measured using a XRF-Avaatech core scanner at EPOC, Bordeaux. Before analysis, the sediment surface was flattened and covered with Ultralene film. The core sections were scanned at a 0.5 cm resolution at two different levels of energy (10 and 30 keV).

In order to easily identify periods in XRF ln(Fe/Ca) record, we computed the cumulative sum (Cusum) of the deviations from the mean:

Cusum = sum(ln(Fe/Ca) - mean(ln(Fe/Ca)))

The Cusum method was developed for industrial control to detect changes in sequential production[32]. More recently, the Cusum has been extensively applied in biological oceanography (e.g. García-Comas et al.[33]) following Ibanez et al.[34]. The Cusum shows periods (i.e., linear sequences) and their value in respect to the long-term average: a positive slope shows a period of values greater than the long-term average, while a negative slope shows a period of values smaller than the long-term average. The steepness of the slope reflects how different a period is from the long-term average. Furthermore, changes in the tendency (i.e., sequential periodical changes in the slope) reflect periodical changes from a set of conditions to another (e.g., a change from a positive slope to a flat slope in the XRF ln(Fe/Ca) record reflects a change from a humid period to a drier period). In the case of the 1 Ma to 0.6 Ma interval, this corresponds to a period of aridification because it is more arid than the previous period between 1.2 Ma to 1 Ma (i.e., there is a change of slope from steep positive to slightly negative). In addition, the period between 1 Ma to 0.6 Ma is very variable because the slope is not straight but noisy. The Cusum can be found under the function name local.trend, in the R package: Pastecs: Package of Analysis of Space-Time Ecological Series.

Plant-wax δD and $\delta^{13}C$: Plant-wax analyses were carried out at MARUM, University of Bremen. Samples were oven dried at 40°C, homogenized and squalane was added as internal standard before extraction. Lipids were extracted with a DIONEX Accelerated Solvent Extractor using a 9:1 mixture of dichloromethane to methanol at 100°C and 1000 psi for five minutes, repeated three times. The saturated hydrocarbon fraction was obtained by elution of the dried lipid extract over a silica column with hexane and subsequent elution over $AgNO_3$-coated silica to remove unsaturated hydrocarbons.
Compound-specific stable carbon isotope ($\delta^{13}C$) analyses were carried out using a ThermoFisher Scientific Trace GC Ultra coupled to a Finnigan MAT 252 isotope ratio monitoring mass spectrometer via a combustion interface operated at 1000°C. Isotope values were calibrated against external CO_2 reference gas and are reported as permille (‰) against the Vienna PeeDee Belemnite (VPDB) standard. Samples were run at least in duplicate. The internal standards yielded a precision of ≤0.3 ‰. Repeated analysis of an external *n*-alkane standard between samples yielded a root-mean-squared accuracy of 0.1 ‰ and a standard deviation of on average 0.2 ‰.
When possible, given the high amount of lipids necessary, compound-specific stable hydrogen isotope (δD) compositions were measured using a ThermoFisher Scientific Trace GC coupled via a pyrolysis reactor operated at 1420°C to a ThermoFisher MAT 253 isotope ratio mass spectrometer. δD values were calibrated against external H_2 reference gas, the 3H+ factor was monitored daily (values vary between 6.7 and 6.9); δD values are reported in permille (‰) versus the Vienna Standard of Mean Ocean Water (VSMOW) standard. The internal standards yielded a precision of 2 ‰ on average. Repeated analysis of an external *n*-

alkane standard between samples yielded a root-mean-squared accuracy of <1 ‰ and a standard deviation of on average 3 ‰.
Results of a method to adjust the δD_{wax} record for vegetation and ice-volume changes is proposed in Extended Data Fig. 4.

Pollen preparation: Samples of 1.5 to 8.5 ml were prepared at MARUM. The volume was measured using water displacement. Samples were decalcified with diluted HCl (~12 %) and treated with HF (~40 %) to remove silicates. Samples were sieved over a screen to remove particles smaller than 10–12 µm. When necessary the sample was decanted to remove remaining silt. Samples were stored in water, mounted in glycerol, and microscopically examined (magnification 400 and 1000x) for pollen and spores. Cyperaceae (sedges) pollen percentages were calculated based on the total number of pollen and spores ranging from 53 to 365 and 95 % confidence intervals were calculated after Maher[35].

$\delta^{18}O$ analyses on foraminifera: Specimens of benthic *Planulina wuellerstorfi* foraminifera were picked from the 250-315 µm size fraction. Analyses were carried out by a coupled system Multiprep-Optima of Micromass© at EPOC. The automated preparation system (Multiprep) transforms carbonate samples into CO_2 gas by treatment with orthophosphoric acid at a constant temperature of 75°C. The CO_2 gas samples were then analysed by isotope mass spectrometry (Optima) in comparison with a calibrated reference gas to determine the isotopic ratio $^{18}O/^{16}O$ of the sample. For all stable oxygen isotope measurements a working standard (Burgbrohl CO_2 gas) was used, which was calibrated against the Vienna Pee Dee Belemnite (VPDB) standard by using the NBS 19 standard. Analytical standard deviation is about 0.05 ‰ ($\pm 1\sigma$).
The chronology of the core was established by tuning the $\delta^{18}O$ benthic foraminifera signal to the reference LR04 stack[36] with the AnalySeries software[37] and yielded a correlation coefficient of R = 0.8 for the last 2.14 Ma. The core is ca. 36 meter long and the sedimentation rate has a mean value of 2 cm/kyr ($\sigma = 0.91$) and is relatively constant.

SSTs reconstruction: *Globigerinoides ruber s. s.* were picked within the 250-315 µm size fraction for trace element analyses. Shells were cleaned at EPOC to eliminate contamination by clays and organic matter based on the procedure of Barker et al.[38]. An Agilent Inductively Coupled Plasma Optical Emission Spectrometer (ICP-OES) was used for magnesium and calcium analyses following the procedure established by De Villiers et al.[39]. Reproducibility obtained from *G. ruber s. s.* on 80 samples from the complete core was better than 6 % ($\pm 1\sigma$, pooled RSD). All new analyses for this study (n = 217) were performed at EPOC. Measured Mg/Ca ratios were converted into temperature values applying the equation established by Anand et al.[40] yielding a precision of 1.2°C.
Total assemblages of planktonic foraminifera were analyzed at EPOC using an Olympus SZH10 binocular microscope following the taxonomy of Hemleben et al.[41] and Kennett et al.[42]. About 300 specimens were counted in each level after splitting with an Otto microsplitter. Relative abundances of species were used to perform quantification of SST after an ecological transfer function[43] developed at EPOC. The method used here is based on the Modern Analogue Techniques (MAT)[44] running under the R software, using a script first developed for dinocyst transfer functions by Guiot and Brewer. The modern database used is composed of 367 core tops and derived from the ones covering the southern Indian Ocean[45] in the MARGO project. Calculations of past hydrological parameters rely on a weighted average of SST values from the best five modern analogues, with a maximum weight given for the

closest analogue in terms of statistical distance, i.e., dissimilarity minimum[43,46]. This method permits the reconstruction of annual SST with a precision of 0.8°C (Extended Data Fig. 7).

As each proxy has some uncertainty related to the calibration, non-temperature influences and lateral advection[15], we applied Empirical Orthogonal Function (EOF) analysis[47] on the two SST records over the last 2.14 Ma (Extended Data Fig. 6). The first Principal Component (PC1) explains 74 % of the total variance for the Mg/Ca and foraminifera transfer function records over the last 2.14 Ma. Correlation between SST proxies and PC1 over the last 2.14 Ma is R= 0.71.

Climate modeling: To investigate the control on the past δD composition of precipitation in the Limpopo catchment we analyzed the results of a transient run with the intermediate complexity isotope-enabled climate model iLOVECLIM[48-50] over the last 150 kyr[51]. The atmospheric part of the coupled climate model was run at T21 spatial resolution (~5.65° lat,lon) and used accelerated forcing (irradiance, GHGs and ice sheets were updated with an acceleration factor 10)[51]. Intermediate complexity models experiences some weaknesses caused by the spatial resolution and simplified convective physics but have the advantage to compute efficiently. iLOVECLIM was previously successfully applied in the Asian monsoon region[51] and in the West African monsoon region[52] to investigate past monsoonal precipitation changes and their links with changes in the isotopic composition of precipitation. For the current study, analysis of its present-day performance for the region together with results over the past 150 kyr are shown in Extended Data Figure 2.

Ecology and environment of the hominins *Paranthropus robustus* and *Australopithecus sediba* in the Limpopo catchment: Building on previous research (e.g., see recent syntheses[53,54]), we produced a short synthesis of multiple lines of evidence to reconstruct the ecology and environmental context of the southern African robust australopith *Paranthropus robustus.* We also discuss briefly *Australopithecus sediba*. Much literature has been devoted to the ecology of the robust australopiths, and particularly the ecological differences between *P. robustus* and *P. boisei*, another species found in eastern Africa. Given the geographic scope of our paper centered on South Africa, we here focus our review mostly on *P. robustus*. The reader should note that it is still a matter of debate whether the robust australopiths, namely *P. robustus, P. boisei*, and *P. aethiopicus* (the likely ancestor of *P. boisei*, also found in eastern Africa) are closely related to each other forming a monophyletic genus, or the robust adaptive traits evolved independently by convergence/parallelism in eastern Africa and southern Africa, making the *Paranthropus* genus diphyletic[54,55]. Authors supporting the diphyletic hypothesis tend to classify the robust australopiths in the genus *Australopithecus*. Until the issue is settled, we use here the genus name *Paranthropus* as a convenient taxonomic label of a grade grouping those three taxa that share similar robust adaptive features that differ from the other more gracile genera *Australopithecus* and *Homo*.

Craniomandibular and dental morphology: species of *Paranthropus* are characterized by a suite of peculiar craniomandibular and dental morphological characters: reduced incisors and canines, molarized premolars, enlarged molars, thick enamel, enlarged insertion areas for temporal muscles, robust mandibular corpus[56]. This suite of robust morphological traits has been frequently interpreted as potential adaptations to diets including hard foods (e.g.,[57,58]). This interpretation is partly supported in *P. robustus* by the dental microwear data that indicate occasional consumption of hard objects (see below). Other authors suggested that

those characters reflect the ability of *Paranthropus* for prolonged chewing of tough plant matter[59,60]. This alternative interpretation is supported by the dental microwear and stable carbon isotopic data in *P. boisei*[61,62]. This interpretation could apply to *P. robustus* as well, even though this species was likely feeding on different kinds of plants (C_4 herbaceous plants in *P. boisei* versus various C_3 and C_4 plants in *P. robustus*, see below).

Potential modern analogs of herbivorous mammals that evolved from omnivorous ancestors with thick enamel and bunodont molars include the giant panda *Ailuropoda melanoleuca* and the red panda *Ailurus fulgens*, both highly specialized independently on a diet of tough bamboo leaves requiring prolonged chewing and numerous repeated chewing cycles (e.g.,[63,64]). Both examples illustrate phylogenetic inertia, with evolution tinkering preexistent morphologies, which limits the range of possible adaptive traits in response to functional selective pressure and results in seemingly suboptimal morphologies for the realized diet. A similar argument was made for *Paranthropus*[53,65]. Therefore, contrary to herbivorous ungulates that evolved long shearing crests and a more lateral mastication to reduce plant matter into small digestible fragments, the giant panda, the red panda, and *Paranthropus* evolved alternative solutions combining a thick enamel and increased dental surface with prolonged use of high masticatory forces.

It was also suggested that an increased dental occlusal surface in mammals could be an adaptive trait for feeding on small bites of small sized food items[66] by increasing the chance of efficiently masticating the food items with a reduced number of chewing cycles, and limiting the wear induced by a strong increased attrition (tooth to tooth contact) in addition to the wear induced by abrasion (tooth to food contact). Similar adaptive traits, most notably enlarged surfaces of third molars, evolved independently multiple times in African herbivorous suids[67].

Compared to *Paranthropus*, the craniomandibular and dental morphology of *A. sediba* is more gracile and more similar to the one found in older species of *Australopithecus* and younger species of *Homo*. It was recently argued that the morphology of the cranium was unsuited for feeding on hard objects[68] while that of the mandible was[69].

Postcranial morphology: very little is known about the postcranial morphology of *P. robustus* but most studies indicate retention of traits adaptive to arboreal climbing (e.g., [70,71]). Hand morphology suggests an ability to perform precision gripping during tool making and using activities[72]. Numerous bone tools are found in Swartkrans Member 3 and Drimolen, sites that yielded numerous specimens of *P. robustus*. Microscopic and macroscopic wear analyses as well as experimental data suggest that those tools were used for digging into termite mounds[73-75]. The scarcity of *Homo* remains compared to those of *P. robustus* in sites bearing the bone tools suggests that the latter species is the most likely tool maker and user[73-75]. *Australopithecus sediba* is known by two partial skeletons that provide numerous information on its postcranial morphology. Its upper limbs and shoulders retain numerous adaptive traits for climbing and suspensory behaviors[76,77].

Microstructure and biomechanics of enamel: a study of the dental microstructure of *P. robustus* indicates that its enamel was decussated (contrary to *P. boisei*[78]), which is assumed to reflect a capacity to withstand strong and/or prolonged biomechanic constraints during mastication. Other mammals feeding on hard objects, such as hyaenids[79], and mammals feeding on tough vegetation, such as many ungulates, also display decussated enamel[80].

In addition, an experimental study on the behavior of enamel under various biomechanic constraints suggests that thick enamel could be an adaptive trait to deal with foods either hard or tough, laden with particulates, potentially including both grit and phytoliths[81]. A recent study observed a low frequency of enamel chipping in *P. robustus*, concluding that it was not adapted to eating hard foods[82], but rather tough vegetation. This interpretation is at odds with the dental microwear data that indicate at least some consumption of hard objects (see below). Alternatively, we argue that it is equally plausible that this low frequency of chipping is related to the specialized decussated microstructure that reinforces the tooth enamel of *P. robustus* at a microscopic scale, making its teeth less prone to chipping and therefore more durable when consuming hard foods, as well as tough foods.

Enamel biogeochemistry: numerous data are available regarding the stable carbon and oxygen isotopic compositions (expressed as $\delta^{13}C$ and $\delta^{18}O$, respectively), and the major elements (Sr, Ba, Ca) of the enamel of *P. robustus*, of other hominins, as well as other contemporaneous animals. The stable carbon isotope ratios enable to quantify the proportions of food items deriving, directly or indirectly (through one or several trophic levels), from C_3 plants (mostly woody vegetation, but also sedges in humid environments) and C_4 plants (mostly grass and sedges, but also shrubs of the Amaranthaceae/Chenopodiaceae family). The $\delta^{13}C$ values of the enamel of *P. robustus* indicate a diet dominated by C_3 plants-derived foods, with a significant proportion (ca. 35-40 %) of C_4 plants-derived foods (Fig. 3B and Extended Data Table 2). Much efforts were dedicated to identify the food items that compose this significant C_4 component in the diet of *P. robustus*[83-86]. Most likely C_4 plants-derived food items include grass leaves and roots, insects such as grasshoppers and termites, small vertebrates consuming C_4 plants or C_4 plants-eating invertebrates (birds, lizards, rodents, small ungulates). Sedges are also considered a likely source of C_4 resources, notably through the consumption of their Undergound Storage Organs (USOs)[87,88]. Sponheimer et al.[84] however argued that C_4 sedges were rather scattered in South African riverine settings and that not many of them produced large palatable USOs. They therefore considered C_4 sedges as a minor food resource for hominins. However, they only studied the sedges from four riverine sites located in the Kruger National Park and it remains unknown whether their conclusions would hold out for the whole Limpopo catchment and larger scales.

More important in our opinion is the fact that the diet of *P. robustus* was dominated by C_3 plants-derived food resources. The latter could include any parts (leaves, stems, fruits, nuts, USOs) of C_3 plants (mostly trees, shrubs, bushes in wooded environments but also abundant sedges in humid environments). Data on the enamel $\delta^{13}C$ values of *A. sediba* are very few (n = 2) but both specimens display low values (-12.1 ‰ and -12.2 ‰) that indicate a diet dominated by C_3 plants-derived food resources[25].

Stable oxygen ratios of enamel are related to multiple factors, including behavior, ecology, diet, physiology, and climate[89]. Levin et al.[90] classified mammals into Evaporation Sensitive (ES) taxa and Evaporation Insensitive (EI) taxa. The $\delta^{18}O$ values in ES taxa increase with aridity. ES taxa do not drink much and get most of the required water from the plants they consume. Conversely, $\delta^{18}O$ values of EI taxa track the $\delta^{18}O$ values of surface water that they drink abundantly and frequently[90,91]. Although hominins were not included into this classification scheme, they are likely water-dependent since all large primates need to drink a lot of water every day. Hominins generally display relatively low $\delta^{18}O$ values on average compared to the rest of the faunas[62,92], suggesting a high water dependence or consumption of

622 plants containing little evaporated water. Those data support the preference of *P. robustus* for
623 wooded and/or humid environments.

624 Intra-tooth variations of $\delta^{13}C$ and $\delta^{18}O$ also inform us about the intra-annual and inter-annual
625 variations in ecology. Such intra-tooth $\delta^{13}C$ and $\delta^{18}O$ profiles were measured using laser
626 ablation on four teeth of *P. robustus* from Swartkrans Member 1[83]. The mean values of the
627 $\delta^{13}C$ profiles are similar to those of other *P. robustus* sampled previously, and they also reveal
628 significant intra-tooth variations with ranges varying from 2 ‰ to 5 ‰ over periods
629 representing approximately one or two years (inferred from the number of perikymata).
630 Significant positive correlations between the $\delta^{13}C$ and $\delta^{18}O$ in three out of four specimens of
631 *P. robustus* also indicate that they consumed relatively more C_4 plants-derived foods during
632 the dry seasons than during the wet seasons[83]. This could suggest an opportunistic sampling of
633 the environment, with a relative consumption of C_3/C_4 plants-derived foods depending partly
634 on seasonal or inter-annual climatic differences. Those data are also congruent with the
635 identification of *P. robustus* as an EI taxon and are similar to the pattern observed in some
636 extant EI herbivorous ungulates (e.g., strong positive correlations of $\delta^{13}C$ and $\delta^{18}O$ profiles in
637 an extant common hippopotamus *Hippopotamus amphibius*[93]).

638 Investigations of trace elements preserved in the enamel of *P. robustus* also revealed
639 interesting patterns[24,94]. *Paranthropus robustus* is characterized by relatively high Sr/Ca
640 ratios, lower than in grazing ungulates, and a bit higher than in carnivores, browsing
641 ungulates, and omnivorous cercopithecid monkeys. Interestingly, *A. africanus* is characterized
642 by even higher Sr/Ca ratios. Both hominins, but especially *A. africanus*, display low Ba/Ca
643 ratios. Altogether, those data indicate a likely low proportion of animal matter in their diets.
644 More interestingly, the only extant animals combining a high Sr/Ca ratio and a low Ba/Ca are
645 the mole rat (*Cryptomys hottentotus*), and to a lesser extent, the common warthog
646 (*Phacochoerus africanus*). Both species consume large amounts of grass roots. This could
647 indicate that grass root consumption was a significant aspect of *P. robustus* diet, explaining
648 part of the C_4 component of the diet. However, the Sr/Ca and the Ba/Ca ratios of *A. africanus*
649 and *P. robustus* are not as extreme as those found in the mole rat and the common warthog,
650 suggesting that the consumption of grass roots was likely not as important as in those two
651 species. As highlighted by Sponheimer et al.[94] one must however stress that the use of major
652 elements concentrations in enamel as an indication of the diet of extant and extinct animals
653 still necessitate further studies. Balter et al.[24] observed Sr/Ca and Ba/Ca ratios for *P. robustus*
654 that are intermediate between those of *A. africanus* and early *Homo*, and similar to those of
655 browsers. They argue the diet of *P. robustus* was dominated by woody plants.

656 **Dental microwear:** investigations of dental microwear also provided useful information to
657 reconstruct the diet of *P. robustus*[61,95-97]. Dental microwear mostly results from a combination
658 of abrasion (food to tooth contact) and attrition (tooth to tooth contact), both resulting in
659 various microscopic scars left at the surface of the enamel facets. Among hominins,
660 specimens of *P. robustus* are characterized by unique microwear textures that display strongly
661 variable complexities, ranging from low to very high values, and low anisotropies. This
662 pattern, originally observed on a few specimens, was later confirmed by a large-scale study of
663 dental microwear in *P. robustus,* including numerous specimens from various sites[98].
664 Similarities in dental microwear textures were noted between *P. robustus* and some specimens
665 of several extant primates that are known to consume hard objects such as nuts and seeds
666 (gray-cheeked mangabeys *Lophocebus albigena,* brown capuchins *Cebus apella*), indicating

667 at least some consumption of hard objects by *P. robustus*. Dental microwear data available for
668 *A. sediba,* although based on two specimens only, also show high complexities, suggesting a
669 potential consumption of hard objects[25].

670 **Stable carbon isotopes of contemporary mammals:** compiled data of $\delta^{13}C$ values for
671 herbivorous mammals that were contemporary and sympatric with *P. robustus* indicate
672 habitats encompassing a mix of C_3 and C_4 plants, suggesting a mix of woodlands and
673 grasslands in all sites that were sampled (data for Swartkrans members 1, 2, and 3[83,84,99,100];
674 Cooper's D[101]; Gondolin[102]; Fig.3B and Extended Data Table 2). The enamel $\delta^{13}C$ values of
675 herbivorous mammals in all *P. robustus*-bearing sites where sufficient data are available
676 display a bimodal distribution (Extended Data Table 2): the main mode indicates that the
677 habitat was dominated by herbivorous mammals consuming mostly C_4 plants, while the
678 secondary mode indicates that a significant portion of the remaining herbivorous mammals
679 consumed C_3 plants. Mammals displaying a strong C_4 signal in their enamel likely consumed
680 herbaceous plants, including mostly dry-adapted C_4 grasses in open habitats and possibly C_4
681 sedges in humid habitats. They are usually classified as grazers. Conversely, mammals
682 displaying a strong C_3 signal in their enamel likely fed mainly on woody plants (trees, shrubs,
683 bushes) in woodlands, and possibly on C_3 sedges in humid habitats. They are usually
684 classified as browsers. Complicating factors of paleodietary reconstructions include the
685 potential consumption of CAM plants (mostly succulents in arid habitats and epiphytic plants
686 in closed forests) and C_4 dicot woody vegetation (e.g., shrubs of the family
687 Amaranthaceae/Chenopodiaceae). However, the classification of mammals using the
688 dichotomy between C_3 browsers and C_4 grazers inferred from $\delta^{13}C$ values is generally
689 confirmed by ecomorphological and dental wear studies[101]. $\delta^{13}C$ data of *P. robustus* are
690 intermediate between the C_4 pole and the C_3 pole, but closer to the latter, indicating a
691 preference of this hominin for the C_3 wooded and/or humid component of its habitat.

692 The enamel $\delta^{13}C$ data of the herbivorous mammals found at the Malapa site with *A. sediba*
693 indicate an environment dominated by C_4 plants, presumably grasses, and a few species
694 consuming C_3 plants, presumably woody plants[25]. The pattern is therefore similar to the one
695 observed in the *P. robustus*-bearing sites, indicating a preference of *A. sediba* for the C_3
696 component, presumably woodland, of the otherwise C_4 grass-dominated landscapes.

697 **Ecomorphology and community structures:** Reed[103] conducted an analysis of the
698 ecological diversity of modern and past faunal communities by quantifying trophic and
699 locomotor adaptive traits of mammals. She found evidence that *P. robustus* inhabited mosaic
700 environments including both woodlands and grasslands, always close to a water source. She
701 also detected a pattern of more open habitats throughout the Swartkrans sequence. This
702 observation supports the information provided by $\delta^{13}C$ values of the herbivorous mammals
703 that, based on our data compilation, generally indicate more C_4 plants in the landscapes,
704 presumably grasses adapted to open and dry environments (Fig. 3B). de Ruiter et al.[104]
705 conducted a correspondence analysis using the relative abundances of the different groups of
706 mammals classified as woodland-adapted and grassland-adapted based on stable carbon
707 isotopes and uniformitarian comparisons to extant relatives. They observed that the relative
708 abundance of *P. robustus* follows relative abundances of woodland-adapted species and is
709 negatively correlated to the relative abundances of grassland-adapted species. Bishop et al.[105]
710 conducted an ecomorphological analysis of bovid postcrania from Sterkfontein Member 5B
711 "Oldowan Infill". They concluded that most bovid species were adapted to open grasslands,

712 and they reconstructed the environment as dominated by grasslands but with a nearby more
713 wooded component. Kuman & Clarke[106] suggested that the absence of *P. robustus* in
714 Sterkfontein Member 5 West could be linked to a drier local habitat without water-dependent
715 species. Overall, those studies indicate that grasslands were important and likely predominant
716 in the environments occupied by *P. robustus*, but always with a more wooded and humid
717 component nearby. The ecological data gained from multiple lines of evidence suggest that *P.*
718 *robustus* preferred that woodland and/or humid component.

719 **Combining the multiple lines of evidence:** based on the aforementioned evidence, we
720 interpret *P. robustus* as a species that was overall ecologically variable (eurytopic), especially
721 in terms of dietary resources, but with a long-lasting preference for the C_3 wooded or humid
722 components of the environments otherwise dominated by C_4 dry-adapted plants. Such a
723 selective feeding behavior, with scarce components of the vegetation that are over-represented
724 in the diet of an animal is frequently observed in extant mammals. For example, extant
725 geladas (*Theropithecus gelada*) from the Guassa Plateau in the Highlands of Ethiopia rely
726 extensively on forbs (ca. 38 % of annual diet, and up to 61 % of monthly diet) although those
727 preferred forbs represent only 8 % of ground cover[107]. A variable C_3-dominated diet,
728 including both hard and tough food items, and displaying strong seasonal or inter-annual
729 variations, is supported by the stable carbon and oxygen isotopes, the dental microwear
730 textures, and the overall morphological adaptive traits displayed by *P. robustus*. The robust
731 craniomandibular and dental traits appear as a reasonable compromise to process efficiently
732 an extremely diversified diet including numerous tough parts of plants along with some hard
733 foods, and probably a lot of small food items that had to be eaten in small bites, with some
734 exogenous grit particulates adhering (e.g., termites, grass roots).

735 The preference of *P. robustus* for habitats dominated by C_3 plants, either in woodlands or in
736 humid environments, is well corroborated by the data gained from the study of other animals,
737 indicating large quantities of C_4 vegetation, but always with a more wooded component and
738 the nearby presence of a water source. Frequent exploitation of the C_4 food resources in the
739 more open component of the landscapes is demonstrated by the stable carbon isotopes that
740 indicate a significant, but not dominant, C_4 component in the diet. Possible use of bone tools
741 and prehensile hands would have enabled *P. robustus* to access a great variety of foods in
742 both wooded and open habitats. *Paranthropus robustus* could be best characterized as an
743 ecotonic species, exploiting intermediate habitats where the edge effect is maximized,
744 enabling it to forage on a maximal variety of foods in both wooded and open habitats within a
745 limited area, while keeping access to secure shelters in woodlands. Such an ecology is
746 displayed by the forest hog (*Hylochoerus meinertzhageni*) that strongly depends on wooded
747 humid forests for shelter, food, and water, but also frequently exploits open grasslands for
748 additional plant resources[108]. Data are scarcer for *A. sediba* but the multiple aforementioned
749 lines of evidence suggest an even stronger preference for C_3 wooded habitats compared to *P.*
750 *robustus*. It is worth noting that similar preference for the C_3 component, presumably
751 woodlands, in overall C_4 grass-dominated landscapes is also documented in several other
752 hominin species from eastern Africa (e.g.,[109,110]).

753 **Extinction of *Paranthropus robustus***

754 It appears likely that the last documented occurrence of *P. robustus* is dated ca. 0.9 Ma, or
755 even later (see Extended Data Table 1). Indeed, multiple lines of dating evidence point to a

young age of Swartkrans Member 3, likely around 0.9 Ma, but possibly as young as 0.6 Ma. It is also worth keeping in mind the frequency of artificial range truncation of extinct taxa, often called the Signor and Lipps effect[111]: due to the imperfect nature of the fossil record, the extinction date of a particular taxon is most probably more recent than the last fossil occurrence of this taxon. Bearing in mind that those authors formulated this caution based on the near-continuous and precisely-dated marine paleontological record, the Signor and Lipps effect is even more pertinent when considering extinction dates based on the spatio-temporally biased continental fossil record of terrestrial faunas (see details in White[112]). This dating uncertainty most probably applies to *P. robustus* as its known geographic distribution is extremely small. Most of the *P. robustus*-bearing sites are located within a circle of ca. 3 km radius, and only Gondolin is located a bit further north, around 25 km from Swartkrans and Sterkfontein. A circle of 12.5 km radius, encompassing all the known occurrences of *P. robustus*, would therefore represent a distribution area of ca. 500 km^2. Large mammals tend to have much larger geographic distributions. For comparison, even the extant species of African great apes with the smallest geographic distribution, the critically endangered eastern gorilla (*Gorilla beringei*), is found over an area of ca. 70000 km^2. Other great apes have much larger distributions (*G. gorilla*: over 700000 km^2; *Pan paniscus*: ca. 156000 km^2; *Pan troglodytes*: over 2600000 km^2; all data from the IUCN website, http://www.iucnredlist.org/). It is therefore most likely that the real distribution area of *P. robustus* was much larger than what is currently sampled by the available fossil record, making the true last occurrence of the species unlikely to be sampled, and the real extinction date of the species likely younger than 0.9 Ma.

The fossil record of South Africa indicates that numerous species became extinct during the Pleistocene. However, the paucity of the record after 1.4 Ma seriously hinders our understanding of the pattern and timing of the extinctions. Middle Pleistocene faunas such as those of Florisbad (ca. 0.25 Ma) are almost entirely composed of species that are similar to the extant species whereas older faunas (e.g., Cornelia at ca. 1 Ma or Elandsfontein at 1 Ma-0.6 Ma) contain a significant proportion of extinct species (e.g., [113]). Neither a precise date nor a time interval (1 Ma-0.5 Ma vs. later during the Pleistocene) can be constrained for the extinction of those species based on their currently available fossil records.

Our new marine record, as well as previously published terrestrial records, are indicative of a clear trend through time toward more open and drier landscapes in the Limpopo catchment. Given that *P. robustus* preferentially thrived in non-dominant C_3 component of its environment (either woodland or humid grassland), and that its diet was dominated by C_3 plants-derived food items, including occasional hard objects, we assume that the regional trend toward a more arid hydroclimate after 1 Ma and the marked precessional variability impacted the abundance of this species and its resilience to environmental changes. As regional hydroclimate became drier, the wooded and humid environments favored by *P. robustus* likely became progressively scarcer, strongly impacting the fitness and survival of the populations of mammals depending on such habitats for food, water, and shelter. We propose a speculative but plausible scenario inspired from the theoretical work by Foley[27]. According to this scenario, the geographic ranges of taxa adapted to woodlands and humid habitats, including *P. robustus*, contracted and expanded according to the precessional ~21 kyr dry and wet cycles. During the multi-millennial dry periods, the range of populations of those taxa contracted and often became fragmented. The resulting isolated populations were especially prone to local extinction through increased competition and predation induced by

the lack of sufficient and suitable food, water, and shelter resources. During multi-millennial wet periods, preferred woodland and humid habitats would have expanded again and the surviving populations would have thrived again and expanded into their previously occupied range, replacing locally extinct populations. The long term trend to aridity, as inferred from our marine record, implies that dry periods became more and more drastic through time, increasing the likelihood for local extinction of numerous local populations, until the extinction of the last remaining local population, and therefore the extinction of the species. Thus both long-term state and the extreme precessional changes in hydroclimate could have impacted the evolution of *P. robustus*. A recent synthesis on factors involved in the extinction in large mammals, spanning three continents and the whole Cenozoic period, concluded that abiotic changes, such as climatic changes, were key players in the extinctions of species[26].

What of *Homo*? Several authors (reviewed in Wood & Strait[114]) suggested that strong morphological, behavioral, and ecological differences between *P. robustus* and the contemporary *Homo* gave an evolutionary advantage to the latter over the former. Some authors therefore related those differences to the extinction of *P. robustus* while *Homo* did not go extinct and remained extremely widespread in Africa and beyond. Strikingly different relative abundances of those two taxa do suggest they were occupying separate ecological niches in the sites where they co-occur (Swartkrans 96 % *P. robustus*, 4 % *Homo*; Drimolen 84 % *P. robustus* 16 % *Homo*, according to Moggi-Cecchi et al.[115]). However, those scenarios are speculative and clearly out of the scope of our paper that is focused on *P. robustus*. Regardless of any potential evolutionary advantage of *Homo* over *P. robustus,* whether or not *Homo* went extinct locally in the Limpopo catchment during the aridification period is meaningless to its subsequent evolutionary history. Remains of *Homo* are indeed known in other parts of South Africa around 1 Ma (e.g., Elandsfontein[116]; Cornelia-Uitzoek[117]), as well as in other parts of Africa[118,119], which would have made any local extinction counterbalanced by subsequent dispersals from other regions. The survival of *Homo* could plausibly be explained solely through plain contingency, especially as recent literature indicates a eurytopic ecology for both *Homo* and *Paranthropus* (Wood & Strait[114]; our synthesis).

Online Content Methods, along with any additional Extended Data display items and Source Data, are available in the online version of the paper; references unique to these sections appear only in the online paper.

842
843
844
845
846
847
848
849

Methods references:

32. Page, E.S. Continuous Inspection Schemes. *Biometrika* **41**, 100–115 (1954).
33. García-Comas, C. *et al.* Zooplankton long-term changes in the NW Mediterranean Sea: Decadal periodicity forced by winter hydrographic conditions related to large-scale atmospheric changes? *J. Marine Syst.* **87**, 216–226 (2011).
34. Ibanez, F., Fromentin, J.M. & Castel, J. Application of the cumulated function to the processing of chronological data in oceanography. *C. R. Acad. Sci. III-Vie* **316**, 745–748 (1993).
35. Maher, L. J., Jr. Nomograms for computing 0.95 confidence limits of pollen data. *Rev. Palaeobot. Palyn.* **13**, 85–93 (1972).
36. Lisiecki, L. E. & Raymo, M. E. A Pliocene-Pleistocene stack of 57 globally distributed benthic $\delta^{18}O$ records. *Paleoceanography* **20**, PA1003 (2005).
37. Paillard, D., Labeyrie, L. D. & Yiou, P. AnalySeries 1.0: Macintosh program performs time-series analysis. *EOS Trans. Am. Geophys. Un.* **77**, 379 (1996).
38. Barker, S., Greaves, M. & Elderfield, H. A study of cleaning procedures used for foraminiferal Mg/Ca paleothermometry. *Geochem. Geophys. Geosyst.* **4**, 8407 (2003).
39. de Villiers, S., Greaves, M. & Elderfield, H. An intensity ratio calibration method for the accurate determination of Mg/Ca and Sr/Ca of marine carbonates by ICP-AES. *Geochem. Geophys. Geosyst.* **3**, 2001GC000169 (2002).
40. Anand, P., Elderfield, H. & Conte, M. H. Calibration of Mg/Ca thermometry in planktonic foraminifera from a sediment trap time series. *Paleoceanography* **18**, 1050 (2003).
41. Hemleben, C., Spindler, M. & Erson, O. R. *Modern Planktonic Foraminifera* (Springer-Verlag, 1989).
42. Kennett, J. P. & Srinivasan, M. S. *Neogene Planktonic Foraminifera: a Phylogenetic Atlas* (Hutchinson Ross, 1983).
43. Guiot, J. & de Vernal, A. in *Proxies in Late Cenozoic Paleoceanography* (eds Hillaire-Marcel, C. & de Vernal, A.) 523–563 (Elsevier, 2007).
44. Kucera, M. in *Proxies in Late Cenozoic Paleoceanography* (eds Hillaire-Marcel, C. & de Vernal, A.) 213–262 (Elsevier, 2007).
45. Barrows, T. T. & Juggins, S. Sea-surface temperatures around the Australian margin and Indian Ocean during the Last Glacial Maximum. *Quat. Sci. Rev.* **24**, 1017–1047 (2005).
46. Kucera, M. *et al.* Reconstruction of sea-surface temperatures from assemblages of planktonic foraminifera: multi-technique approach based on geographically constrained calibration data sets and its application to glacial Atlantic and Pacific Oceans. *Quat. Sci. Rev.* **24**, 951–998 (2005).
47. Von Storch, H. & Zwiers, F. W. *Statistical Analysis in Climate Research* (Cambridge University Press, 1999).
48. Roche, D. M. $\delta^{18}O$ water isotope in the iLOVECLIM model (version 1.0)–Part 1: Implementation and verification. *Geosci. Model Dev.* **6**, 1481–1491 (2013).
49. Roche, D. M. & Caley, T. $\delta^{18}O$ water isotope in the iLOVECLIM model (version 1.0)–Part 2: Evaluation of model results against observed $\delta^{18}O$ in water samples. *Geosci. Model Dev.* **6**, 1493–1504 (2013).
50. Caley, T. & Roche, D. M. $\delta^{18}O$ water isotope in the iLOVECLIM model (version 1.0)–Part 3: A palaeo-perspective based on present-day data–model comparison for oxygen stable isotopes in carbonates. *Geosci. Model Dev.* **6**, 1505–1516 (2013).

51. Caley, T., Roche, D. M., & Renssen, H. Orbital Asian summer monsoon dynamics revealed using an isotope-enabled global climate model. *Nat. Commun.* **5**, 5371 (2014).
52. Collins, J. A. *et al.* Rapid termination of the African Humid Period triggered by northern high-latitude cooling. *Nat. Commun.* **8**, 1372 (2017).
53. Grine, F. E. & Daegling, D. J. Functional morphology, biomechanics and the retrodiction of early hominin diets. *C. R. Palevol* **16**, 613–631 (2017).
54. Wood, B. & Schroer, K. *in Human Paleontology and Prehistory. Contributions in Honor of Yoel Rak* (eds Marom, A. & Hovers, E.) 95–107 (Springer, 2017).
55. Patterson, D. B., Faith, J. T., Bobe, R. & Wood, B. Regional diversity patterns in African bovids, hyaenids, and felids during the past 3 million years: the role of taphonomic bias and implications for the evolution of *Paranthropus*. *Quat. Sci. Rev.* **96**, 9–22 (2014).
56. Grine, F. E. (ed) *Evolutionary History of the "Robust" Australopithecines* (Aldine de Gruyter, 1988).
57. Strait D. S. *et al.* Viewpoints: Diet and dietary adaptations in early hominins: the hard food perspective. *Am. J. Phys. Anthropol.* **151**, 339–355 (2013).
58. Smith, A. L. *et al.* The feeding biomechanics and dietary ecology of *Paranthropus boisei*. *Anat. Rec.* **298**, 145–167 (2015).
59. Rabenold, D. & Pearson, O. M. Abrasive, silica phytoliths and the evolution of thick molar enamel in primates, with implications for the diet of *Paranthropus boisei*. *PLOS ONE* **6**, e28379 (2011).
60. Scott, J. E., McAbee, K. R., Eastman, M. M. & Ravosa, M. J. Experimental perspective on fallback foods and dietary adaptations in early hominins. *Biol. Letters* **10**, 20130789 (2014).
61. Ungar, P. S., Grine, F. E. & Teaford, M. F. Dental microwear and diet of the Plio-Pleistocene hominin *Paranthropus boisei*. *PLOS ONE* **3**, e2044 (2008).
62. Cerling, T. E. *et al.* Diet of *Paranthropus boisei* in the early Pleistocene of East Africa. *Proc. Natl Acad. Sci. USA* **108**, 9337–9341 (2011).
63. King, R. A. *Using* Ailuropoda melanoleuca *as a Model Species for Studying the Ecomorphology of Paranthropus*. Master thesis, Marshall University (2014).
64. Weng, Z. Y. *et al.* Giant panda′s tooth enamel: structure, mechanical behavior and toughening mechanisms under indentation. *J. Mech. Behav. Biomed.* **64**, 125–138 (2016).
65. Ungar, P. S. & Hlusko, L. J. The evolutionary path of least resistance. *Science* **353**, 29–30 (2016).
66. Lucas, P. W. *Dental Functional Morphology: How Teeth Work* (Cambridge University Press, 2004).
67. Souron, A. *in Ecology, Conservation and Management of Wild Pigs and Peccaries* (eds Melletti, M. & Meijaard, E.) 29–38 (Cambridge University Press, 2017).
68. Ledogar, J. A. *et al.* Mechanical evidence that *Australopithecus sediba* was limited in its ability to eat hard foods. *Nat. Commun.* **7**, 10596 (2016).
69. Daegling, D. J., Carlson, K. J., Tafforeau, P., de Ruiter, D. J., & Berger, L. R. Comparative biomechanics of *Australopithecus sediba* mandibles. *J. Hum. Evol.* **100**, 73–86 (2016).
70. Grine, F. E. & Susman, R. L. Radius of *Paranthropus robustus* from member 1, Swartkrans formation, *South Africa. Am. J. Phys. Anthropol.* **84**, 229–248 (1991).
71. Patel, B. A. The hominoid proximal radius: re-interpreting locomotor behaviors in early hominins. *J. Hum. Evol.* **48**, 415–432 (2005).

72. Susman, R. L. Hand of *Paranthropus robustus* from Member 1, Swartkrans: fossil evidence for tool behavior. *Science* **240**, 781–784 (1988).
73. Backwell, L. R. & d'Errico, F. Additional evidence on the early hominid bone tools from Swartkrans with reference to spatial distribution of lithic and organic artefacts. *S. Afr. J. Sci.* **99**, 259–267 (2003).
74. Backwell, L. R. & d'Errico, F. Early hominid bone tools from Drimolen, South Africa. *J. Archaeol. Sci.* **35**, 2880–2894 (2008).
75. d'Errico, F. & Backwell, L. R. Assessing the function of early hominin bone tools. *J. Archaeol. Sci.* **36**, 1764–1773 (2009).
76. Churchill, S. E. *et al.* The upper limb of *Australopithecus sediba*. *Science* **340**, 1233477 (2013).
77. Rein, T. R., Harrison, T., Carlson, K. J. & Harvati, K. Adaptation to suspensory locomotion in *Australopithecus sediba*. *J. Hum. Evol.* **104**, 1–12 (2017).
78. Macho, G. *in Trends in Biological Anthropology*. Volume 1 (eds Gerdau-Radonić, K. & McSweeney, K.) 1–10 (Oxbow Books, 2015).
79. Tseng, Z. J. Connecting Hunter-Schreger Band microstructure to enamel microwear features: new insights from durophagous carnivores. *Acta Palaeontol. Pol.* **57**, 473–484 (2012).
80. Alloing-Séguier, L., Lihoreau, F., Boisserie, J.-R., Charruault, A.-L., Orliac, M. & Tabuce, R. Enamel microstructure evolution in anthracotheres (Mammalia, Cetartiodactyla) and new insights on hippopotamoid phylogeny. *Zool. J. Linn. Soc. 171*, 668–695 (2014).
81. Constantino, P. J., Borrero-Lopez, O., Pajares, A. & Lawn, B. R. Simulation of enamel wear for reconstruction of diet and feeding behavior in fossil animals: a micromechanics approach. *BioEssays* **38**, 89–99 (2016).
82. Towle, I., Irish, J. D. & De Groote, I. Behavioral inferences from the high levels of dental chipping in *Homo naledi*. *Am. J. Phys. Anthropol.* **164**, 184–192 (2017).
83. Sponheimer, M. *et al.* Isotopic evidence for dietary variability in the early hominin *Paranthropus robustus*. *Science* **314**, 980–982 (2006).
84. Sponheimer, M. *et al.* Hominins, sedges, and termites: new carbon isotope data from the Sterkfontein valley and Kruger National Park. *J. Hum. Evol.* **48**, 301–312 (2005).
85. Sponheimer, M. & Lee-Thorp, J. A. Differential resource utilization by extant great apes and australopithecines: towards solving the C_4 conundrum. *Comp. Biochem. Phys. A* **136**, 27–34 (2003).
86. Sponheimer, M. *in The Paleobiology of Australopithecus* (eds Reed, K. E., Fleagle, J. G. & Leakey, R. E.) 225–233 (Springer, 2013).
87. Dominy, N. J., Vogel, E. R., Yeakel, J. D., Constantino, P. & Lucas, P. W. Mechanical properties of plant underground storage organs and implications for dietary models of early hominins. *Evol. Biol.* **35**, 159–175 (2008).
88. Yeakel, J. D., Dominy, N. J., Koch, P. L. & Mangel, M. Functional morphology, stable isotopes, and human evolution: a model of consilience. *Evolution* **68**, 190–203 (2014).
89. Sponheimer, M. & Lee-Thorp, J. A. Oxygen isotopes in enamel carbonate and their ecological significance. *J. Archaeol. Sci.* **26**, 723–728 (1999).
90. Levin, N. E., Cerling, T. E., Passey, B. H., Harris, J. M. & Ehleringer, J. R. A stable isotope aridity index for terrestrial environments. *Proc. Natl Acad. Sci. USA* **103**, 11201–11205 (2006).
91. Faith, J. T. Paleodietary change and its implications for aridity indices derived from $\delta^{18}O$ of herbivore tooth enamel. *Palaeogeogr. Palaeoclimatol. Palaeoecol.* **490**, 571–578 (2018).

92. Lee-Thorp, J. A., Sponheimer, M., Passey, B. H., de Ruiter, D. J. & Cerling, T. E. Stable isotopes in fossil hominin tooth enamel suggest a fundamental dietary shift in the Pliocene. *Philos. T. Roy. Soc. B* **365**, 3389–3396 (2010).
93. Souron, A., Balasse, M. & Boisserie, J.-R. Intra-tooth isotopic profiles of canines from extant *Hippopotamus amphibius* and late Pliocene hippopotamids (Shungura Formation, Ethiopia): insights into the seasonality of diet and climate. *Palaeogeogr. Palaeoclimatol. Palaeoecol.* **342–343**, 97–110 (2012).
94. Sponheimer, M., de Ruiter, D., Lee-Thorp, J. & Späth, A. Sr/Ca and early hominin diets revisited: new data from modern and fossil tooth enamel. *J. Hum. Evol.* **48**, 147–156 (2005).
95. Ungar, P. S. & Sponheimer, M. The diets of early hominins. *Science* **334**, 190–193 (2011).
96. Grine, F. E., Sponheimer, M., Ungar, P. S., Lee-Thorp, J. & Teaford, M. F. Dental microwear and stable isotopes inform the paleoecology of extinct hominins. *Am. J. Phys. Anthropol.* **148**, 285–317 (2012).
97. Ungar, P. S., Scott, J. R. & Steininger, C. M. Dental microwear differences between eastern and southern African fossil bovids and hominins. *S. Afr. J. Sci.* **112**, 1–5 (2016).
98. Peterson, A. S. *Dental Microwear Textures of Paranthropus robustus from Kromdraai, Drimolen, and an Enlarged Sample from Swartkrans: Ecological and Intraspecific Variation.* Master thesis, University for Arkansas (2017).
99. Lee-Thorp, J. A., van der Merwe, N. J. & Brain, C. K. Diet of *Australopithecus robustus* at Swartkrans from stable carbon isotopic analysis. *J. Hum. Evol.* **27**, 361–372 (1994).
100. Lee-Thorp, J., Thackeray, J. F. & van der Merwe, N. The hunters and the hunted revisited. *J. Hum. Evol.* **39**, 565–576 (2000).
101. Steininger, C. M. *The dietary behaviour of early Pleistocene bovids from Cooper's Cave and Swartkrans, South Africa*. PhD thesis, University of the Witwatersrand (2011).
102. Adams, J. W. Stable carbon isotope analysis of fauna from the Gondolin GD 2 fossil assemblage, South Africa. *Ann. Ditsong Natl Mus. Nat. Hist.* **2**, 1–5 (2012).
103. Reed, K. E. Early hominid evolution and ecological change through the African Plio-Pleistocene. *J. Hum. Evol.* **32**, 289–322 (1997).
104. de Ruiter, D. J., Sponheimer, M. & Lee-Thorp, J. A. Indications of habitat association of *Australopithecus robustus* in the Bloubank Valley, South Africa. *J. Hum. Evol.* **55**, 1015–1030 (2008).
105. Bishop, L. C., Pickering, T., Plummer, T. & Thackeray, F. Paleoenvironmental setting for the Oldowan industry at Sterkfontein. *Paper presented at the XVth International Congress of the International Union for Quaternary Research, The Environmental Background to Hominid Evolution in Africa, Durban* (1999).
106. Kuman, K. & Clarke, R. J. Stratigraphy, artefact industries and hominid associations for Sterkfontein, Member 5. *J. Hum. Evol.* **38**, 827–847 (2000).
107. Fashing, P. J., Nguyen, N., Venkataraman, V. V. & Kerby, J. T. Gelada feeding ecology in an intact ecosystem at Guassa, Ethiopia: variability over time and implications for theropith and hominin dietary evolution. *Am. J. Phys. Anthropol.* **155**, 1–16 (2014).
108. d'Huart, J.-P. in *Pigs, Peccaries, and Hippos : Status Survey and Conservation Action Plan* (ed. Oliver, W. L. R.) 84–92 (IUCN, 1993).

109. Quinn, R. L. *et al.* Pedogenic carbonate stable isotopic evidence for wooded habitat preference of early Pleistocene tool makers in the Turkana Basin. *J. Hum. Evol.* **65**, 65–78 (2013).
110. Robinson, J. R., Rowan, J., Campisano, C. J., Wynn, J. G. & Reed, K. E.. Late Pliocene environmental change during the transition from *Australopithecus* to *Homo*. *Nature Ecol. Evol.* **1**, 0159 (2017).
111. Signor, P. W., III & Lipps, J. H. in *Geological Implications of Impacts of Large Asteroids and Comets on the Earth* (eds Silver, L. T. & Schultz, P. H.) 291–296 (The Geological Society of America, 1982).
112. White, T. D. in *Paleoclimate and Evolution, with Emphasis on Human Origins* (eds Vrba, E. S., Denton, G. H., Partridge, T. C. & Burckle, L. H.) 369–384 (Yale University Press, 1995).
113. Codron, D., Brink, J. S., Rossouw, L. & Clauss, M. The evolution of ecological specialization in southern African ungulates: competition-or physical environmental turnover? *Oikos* **117**, 344–353 (2008).
114. Wood, B. & Strait, D. Patterns of resource use in early *Homo* and *Paranthropus*. *J. Hum. Evol.* **46**, 119–162 (2004).
115. Moggi-Cecchi, J., Menter, C., Boccone, S. & Keyser, A. Early hominin dental remains from the Plio-Pleistocene site of Drimolen, South Africa. *J. Hum. Evol.* **58**, 374–405 (2010).
116. Klein, R. G., Avery, G., Cruz-Uribe, K. & Steele, T. E. The mammalian fauna associated with an archaic hominin skullcap and later Acheulean artifacts at Elandsfontein, Western Cape Province, South Africa. *J. Hum. Evol.* **52**, 164–186 (2007).
117. Brink, J. S. *et al.* First hominine remains from a~ 1.0 million year old bone bed at Cornelia-Uitzoek, Free State Province, South Africa. *J. Hum. Evol.* **63**, 527–535 (2012).
118. Asfaw, B. *et al.* Remains of *Homo erectus* from Bouri, Middle Awash, Ethiopia. *Nature* **416**, 317–320 (2002).
119. Abbate, E. *et al.* A one-million-year-old *Homo* cranium from the Danakil (Afar) Depression of Eritrea. *Nature* **393**, 458–460 (1998).
120. Bahr, A. *et al.* Deciphering bottom current velocity and paleoclimate signals from contourite deposits in the Gulf of Cádiz during the last 140 kyr: an inorganic geochemical approach. *Geochem. Geophys. Geosyst.* **15**, 3145–3160 (2014).
121. Adegbie, A. T., Schneider, R. R., Röhl, U. & Wefer, G. Glacial millennial-scale fluctuations in central African precipitation recorded in terrigenous sediment supply and freshwater signals offshore Cameroon. *Palaeogeogr. Palaeoclimatol. Palaeoecol.* **197**, 323–333 (2003).
122. Dickson, A. J., Leng, M. J., Maslin, M. A. & Röhl, U. Oceanic, atmospheric and ice-sheet forcing of South East Atlantic Ocean productivity and South African monsoon intensity during MIS-12 to 10. *Quat. Sci. Rev.* **29**, 3936–3947 (2010).
123. Revel, M. *et al.* 20,000 years of Nile River dynamics and environmental changes in the Nile catchment area as inferred from Nile upper continental slope sediments. *Quat. Sci. Rev.* **130**, 200–221 (2015).
124. Ziegler, M. *et al.* Development of Middle Stone Age innovation linked to rapid climate change. *Nat. Commun.* **4**, 1905 (2013).
125. Rohling, E. J. *et al.* Sea-level and deep-sea-temperature variability over the past 5.3 million years. *Nature* **508**, 477–482 (2014).

126. IAEA. *Isotope Hydrology Information System, The ISOHIS Database* (available at: http://www.iaea.org/water, 2006, last access: 8 March 2012).
127. Risi, C., Bony, S. & Vimeux, F. Influence of convective processes on the isotopic composition ($\delta^{18}O$ and δD) of precipitation and water vapor in the tropics: 2. Physical interpretation of the amount effect. *J. Geophys. Res.* **113**, D19306 (2008).
128. Stock, W. D., Chuba, D. K. & Verboom, G. A. Distribution of South African C_3 and C_4 species of Cyperaceae in relation to climate and phylogeny. *Austral Ecol.* **29**, 313–319 (2004).
129. Dupont, L. M. & Kuhlmann, H. Glacial-interglacial vegetation change in the Zambezi catchment. *Quat. Sci. Rev.* **155**, 127–135 (2017).
130. Schrag, D. P. *et al.* The oxygen isotopic composition of seawater during the Last Glacial Maximum. *Quat. Sci. Rev.* **21**, 331–342 (2002).
131. Sachse, D. *et al.* Molecular paleohydrology: interpreting the hydrogen-isotopic composition of lipid biomarkers from photosynthesizing organisms. *Annu. Rev. Earth Planet. Sci.* **40**, 221–249 (2012).
132. Collins, J. A. *et al.* Estimating the hydrogen isotopic composition of past precipitation using leaf-waxes from western Africa. *Quat. Sci. Rev.* **65**, 88–101 (2013).
133. Schefuß, E., Schouten, S., Jansen, J. F. & Sinninghe Damsté, J. S. African vegetation controlled by tropical sea surface temperatures in the mid-Pleistocene period. *Nature* **422**, 418–421 (2003).
134. Grinsted, A. Moore, J. C. & Jevrejeva, S. Application of the cross wavelet transform and wavelet coherence to geophysical time series. *Nonlinear Process. Geophys.* **11**, 561–566 (2004).
135. Schulz, M. & Mudelsee, M. REDFIT: estimating red-noise spectra directly from unevenly spaced paleoclimatic time series. *Comput. Geosci.* **28**, 421–426 (2002).
136. Imbrie, J. *et al.* in *Milankovitch and Climate: Understanding the Response to Astronomical Forcing* (eds Berger, A. *et al.*) 269–305 (D. Reidel Publishing Company, 1984).
137. Dirks, P. H. *et al.* Geological setting and age of *Australopithecus sediba* from southern Africa. *Science* **328**, 205–208 (2010).
138. Pickering, R. *et al. Australopithecus sediba* at 1.977 Ma and implications for the origins of the genus *Homo*. *Science* **333**, 1421–1423 (2011).
139. Berger, L. R., de Ruiter, D. J., Steininger, C. M. & Hancox, J. Preliminary results of excavations at the newly investigated Coopers D deposit, Gauteng, South Africa. *S. Afr. J. Sci.* **99**, 276–278 (2003).
140. de Ruiter, D. J. *et al.* New *Australopithecus robustus* fossils and associated U-Pb dates from Cooper's cave (Gauteng, South Africa). *J. Hum. Evol.* **56**, 497–513 (2009).
141. Keyser, A. W., Menter, C. G., Moggi-Cecchi, J., Pickering, T. R. & Berger, L. R. Drimolen: a new hominid-bearing site in Gauteng, South Africa. *S. Afr. J. Sci.* **96**, 193–197 (2000).
142. Adams, J. W., Rovinsky, D. S., Herries, A. I. & Menter, C. G. Macromammalian faunas, biochronology and palaeoecology of the early Pleistocene Main Quarry hominin-bearing deposits of the Drimolen Palaeocave System, South Africa. *PeerJ* **4**, e1941 (2016).
143. Thackeray, J. F., Kirschvink, J. L. & Raub, T. D. Palaeomagnetic analyses of calcified deposits from the Plio-Pleistocene hominid site of Kromdraai, South Africa: news & views. *S. Afr. J. Sci.* **98**, 537–540 (2002).

144. Herries, A. I., Curnoe, D. & Adams, J. W. A multi-disciplinary seriation of early *Homo* and *Paranthropus* bearing palaeocaves in southern Africa. *Quat. Int.* **202**, 14–28 (2009).
145. Herries, A. I. & Adams, J. W. Clarifying the context, dating and age range of the Gondolin hominins and *Paranthropus* in South Africa. *J. Hum. Evol.* **65**, 676–681 (2013).
146. Braga, J., Fourvel, J.-B., Lans, B., Bruxelles, L. & Thackeray, J. F.in *Kromdraai. A birthplace of* Paranthropus *in the Cradle of Humankind* (eds Braga, J. & Thackeray, J. F.) 1–16 (SUN PRESS, 2016).
147. Herries, A. I., Adams, J. W., Kuykendall, K. L. & Shaw, J. Speleology and magnetobiostratigraphic chronology of the GD 2 locality of the Gondolin hominin-bearing paleocave deposits, North West Province, South Africa. *J. Hum. Evol.* **51**, 617–631 (2006).
148. Adams, J. W., Herries, A. I., Kuykendall, K. L. & Conroy, G. C. Taphonomy of a South African cave: geological and hydrological influences on the GD 1 fossil assemblage at Gondolin, a Plio-Pleistocene paleocave system in the Northwest Province, South Africa. *Quat. Sci. Rev.* **26**, 2526–2543 (2007).
149. Curnoe, D. K. A. *Contribution to the question of early* Homo *in southern Africa: researches into dating, taxonomy and phylogeny reconstruction*. PhD thesis, Australian National University (1999).
150. Herries, A. I. & Shaw, J. Palaeomagnetic analysis of the Sterkfontein palaeocave deposits: Implications for the age of the hominin fossils and stone tool industries. *J. Hum. Evol.* **60**, 523–539 (2011).
151. Granger, D. E. *et al.* New cosmogenic burial ages for Sterkfontein Member 2 *Australopithecus* and Member 5 Oldowan. *Nature* **522**, 85–88 (2015).
152. Gibbon, R. J. *et al.* Cosmogenic nuclide burial dating of hominin-bearing Pleistocene cave deposits at Swartkrans, South Africa. *Quat. Geochronol.* **24**, 10–15 (2014).
153. Curnoe, D., Grün, R., Taylor, L. & Thackeray, F. Direct ESR dating of a Pliocene hominin from Swartkrans. *J. Hum. Evol.* **40**, 379–391 (2001).
154. Pickering, R., Kramers, J. D., Hancox, P. J., de Ruiter, D. J. & Woodhead, J. D. Contemporary flowstone development links early hominin bearing cave deposits in South Africa. *Earth Planet. Sc. Lett.* **306**, 23–32 (2011).
155. Balter, V. *et al.* U-Pb dating of fossil enamel from the Swartkrans Pleistocene hominid site, South Africa. *Earth Planet. Sc. Lett.* **267**, 236–246 (2008).
156. Vrba, E. S. Some evidence of chronology and palaeoecology of Sterkfontein, Swartkrans and Kromdraai from the fossil Bovidae. *Nature* **254**, 301–304 (1975).
157. Vrba, E. S. in *L'environnement des hominidés au Plio-Pléistocène* (eds Beden, M. *et al.*) 345–369 (Masson, 1985).
158. Churcher, C. S. & Watson, V. Additional fossil Equidae from Swartkrans. Swartkrans: a cave's chronicle of early man. *Pretoria: Transvaal Museum* **8**,137–150 (1993).
159. Blackwell, B. A. Problems associated with reworked teeth in electron spin resonance (ESR) dating. *Quat. Sci. Rev.* **13**, 651–660 (1994).
160. Steininger, C. Local ecological profile for *Paranthropus robustus* in South Africa using stable carbon isotopes from associated bovid teeth. *Quat. Int.* **279**, 466 (2012).

Extended data legends:

Extended Data Figure 1: ln(Fe/Ca) as a proxy for Limpopo runoff. Ca and Fe are both elements with complex and multiple origins in marine sediments. Fe could be related with redox variations, detrital and fluvial input, among others while Ca can be related with the biogenic fraction (foraminifera, nannofossils) and detrital input. In order to properly interpret the ln(Fe/Ca) ratio at our study location we applied principal components analysis[120] (PCA). a) The first principal component (PC1) describes 66 % of the total variance for the entire site MD96-2048. The negative loadings for PC1 are Ca and Sr while all other elements (Al, Si, K, Ti, Fe and Zr) have positive loadings. Ca and Sr are elements associated with biogenic carbonate and are mainly related to presence of foraminifera. Element matrix correlation shows a strong positive linear correlation ($R > +0.70$) between Fe and typically detrital elements as Al, Si, Ti and K. Ca shows negative correlation with Fe ($R = -0.5$).
b) ln(Fe/Ca) show a strong correlation with PC1 ($R = 0.94$) and a strong relationship with Limpopo runoff proxies (Extended Data Fig. 3). Fe and Ti elements are related to terrigenous and siliciclastic components (heavy minerals, oxides) and the carbonate content (Ca) variation is mainly due to dilution by terrigenous sediment. ln(Fe/Ca) is therefore a proxy of Limpopo runoff in agreement with previous studies in riverine basins along the African continent[10,121-124].
To confirm a weak influence of sea level changes on the Fe/Ca record we compared our ln (Fe/Ca) record with the deep-water $\delta^{18}O$ component for relative sea level reconstructed by Rohling et al.,[125] (bottom on b)). Both records are plotted against the LR04 chronology. Visual inspection and statistical test do not support a dominant effect of sea level changes on the ln(Fe/Ca) record ($R = 0.05$). PC3, that describes 11 % of the total variance for the entire site MD96-2048, is closely related to sea level changes. The negative loadings for PC3 are mainly Sr and to a lesser degree K and Ti while the main positive loadings are Zr and to a lesser degree Si.

Extended Data Figure 2: Control on the δD composition of precipitation in the Limpopo catchment. a) Seasonal δD composition of precipitation and b) precipitation at Pretoria station[126] in comparison to the iLOVECLIM model results at the corresponding latitude and longitude[48,49]. All data are centered around their annual average. Depleted δD values are indicative of increasing amounts of rainfall[127]. c) Results of the transient simulation with the isotope enabled numerical climate model iLOVECLIM for the δD composition of precipitation and precipitation in the Limpopo catchment (~ -27.5°S to -22°S and 30°E to 36°E) over the last 150 kyr (Methods)[51]. Black curves show the results after filtering with a low pass filter. The δD composition of precipitation and precipitation amount in the Limpopo catchment are negatively correlated ($R = -0.63$, p-value$<< 0.001$) over the last 150 kyr. Maxima of precipitation are phased with maxima in austral summer insolation at 30°S and lead to more depleted $\delta D_{precipitation}$ (amount effect).

Extended Data Figure 3: Relationship between Limpopo runoff, local Southern Hemisphere insolation and the C_{31} *n*-alkane $\delta^{13}C$ record over the last 800 kyr. a) Comparison between the ln(Fe/Ca) XRF signal and austral summer local insolation at 30°S[31]. b) Comparison between the ln(Fe/Ca) XRF signal and the branched glycerol dialkyl glycerol tetraethers (brGDGT) concentration in the sediment[15]. brGDGT are commonly found in soil and can be attributed to Limpopo River runoff[15]. c) Comparison between the ln(Fe/Ca) XRF signal and the C_{31} *n*-alkane $\delta^{13}C$ record[16]. More Limpopo River discharge is associated with more C_4 plant input and increase in austral summer insolation at 30°S. d) Comparison

between inverted ln(Fe/Ca) XRF signal and the accumulation rate (AR) of $CaCO_3$ as a measure of biogenic carbonate. The ln(Fe/Ca) XRF record is not primarily controlled by dilution due to biological productivity (R = 0.1).

A previous study on core MD96-2048 over the last 0.8 Ma interpreted shifts towards more depleted $\delta^{13}C_{wax}$ as potentially reflecting more humid conditions[16]. However, the anti-correlation between $\delta^{13}C_{wax}$ and δD_{wax} values (Extended Data Fig. 4) in our study indicates that enriched $\delta^{13}C_{wax}$ values are associated with more humid conditions. Because C_4 plants in the Limpopo catchment are dominant in the interior (Fig. 1), we propose that more enriched $\delta^{13}C_{wax}$ values indicate a higher relative contribution from more upstream sources (more C_4) during times of high runoff compared to only downstream sources (more C_3) during low discharge. In addition, humid conditions would have favored the extension of sedge-rich vegetation (Cyperaceae, of which 20 to 60 % are C_4 plants in this region[128]) in riverine swamps and floodplains along the river course, explaining the detected increase in Cyperaceae pollen at times of increased fluvial discharge (Fig. 2). Studies on sediments from the adjacent Zambezi catchment similarly suggest the extension of swampy sedge-rich vegetation including C_4-Cyperaceae when river discharge was high and infer that more C_4 plant waxes are exported to the ocean when flooding of floodplains occurs during rainfall maxima[10,129].

Extended Data Figure 4: Relation between the $\delta^{13}C$ C_{31} *n*-alkanes record and the δD C_{31} *n*-alkanes record. A. Correlation between the $\delta^{13}C$ C_{31} *n*-alkanes record and the δD C_{31} *n*-alkanes record with or without vegetation and ice volume correction (vc-ivf) over the last 2.14 Ma (n = 19). An anti-correlation exists between the $\delta^{13}C$ and the δD signals of the C_{31} *n*-alkanes. The C_{31} *n*-alkane is used because it is the most abundant homologue in the samples. B. Raw $\delta^{13}C_{wax}$, δD_{wax} data and δD_{wax} adjusted for ice-volume and vegetation changes from core MD96-2048. Mean analytical uncertainties are indicated. a) $\delta^{13}C_{wax}$ of the C_{31} homologue (Castaneda et al.[16] in light green and this study in dark green). b) δD_{wax} of the C_{31} homologue. c) δD_{wax} of the C_{31} homologue adjusted for ice volume changes (ivf) using a seawater $\delta^{18}O$ curve[125] and converting to δD assuming a Last Glacial Maximum (LGM) increase of 7.2‰. We use 7.2‰ because sediment pore water $\delta^{18}O$ and δD measurements suggest that the glacial ocean δD increase has a mean value of 7.2‰[130]. We also adjusted the δD_{wax} record for vegetation changes (vc) using published fractionation factors (-123‰ ± 31‰ for C_3 trees, -139‰ ± 27‰ for C_4 grasses[131]) and the $\delta^{13}C_{wax}$ signal following the procedure developed by Collins et al.[132]. End-member $\delta^{13}C_{wax}$ values used for C_3 and C_4 vegetation were -36‰ and -21.5‰, respectively[133]. The error ranges for the vegetation fractionation factors are very large[131]. They derive from the compilation of a global dataset from individual plants which is not comparable to an ecosystem fractionation in a specific catchment such in the Limpopo that will fractionate with a much smaller uncertainty. As we, however, do not know the exact fractionation factor in the Limpopo catchment and regard the uncertainties from the global compilation as unrealistic for a specific ecosystem we refrained from propagating this uncertainty into the vegetation corrections. The vegetation and ice-volume adjusted δD_{wax} record is very similar to the unadjusted record, highlighting that the adjustments have a minor effect.

Extended Data Figure 5: Statistical analyses for the ln Fe/Ca XRF record and PC1 SST record. a) Spectral power for ln(Fe/Ca) by wavelet analysis realized with the MatLab package of Grinsted et al.[134]. The thick contour designates the 5 % significance level against red noise. Dash black lines indicate the variability at the precession, obliquity and eccentricity periods. b) Spectral analysis of ln Fe/Ca with REDFIT[135]. Red line show the false-alarm level at the 95 % confidence interval. Spectral peaks exceeding the false-alarm level can be

considered significant[135]. c) Blackman-Tukey cross correlation between ln(Fe/Ca) XRF and ETP realized with the Analyseries software[37] over the last 2.14 Ma. ETP is constructed by normalizing and stacking Eccentricity, Tilt (obliquity) and negative Precession to evaluate coherence and phase (timing) relative to orbital extremes[136]. Red curve shows the spectral power for ln Fe/Ca record. Black curve show the spectral power for ETP. The coherency (which varies between 0 and 1) is represented by the grey curve and gives the interval within which the spectrum is significant. In our case, the non-zero coherency is higher than 0.55 and is significant at the 95 % confidence interval (grey line). There are significant spectral peaks for eccentricity and precession but not for obliquity. The ln(Fe/Ca) XRF record and ETP are in phase at the 400 kyr period, the eccentricity leads by 16 kyr the ln(Fe/Ca) record at the 100 kyr period and the ln(Fe/Ca) record is in anti-phase with negative precession (in-phase with positive precession) at the 19 and 23 kyr periods. The three statistical analyses are in agreement and indicate significant variability at the 400, 100, 23 and 19 kyr periods and insignificant variability at 41 kyr period. d) Comparison between the precessional component of the ln(Fe/Ca) record (Gaussian filter frequency 1/23 000; bandwidth: 5e-06) obtained with the Analyseries software[37] and the precession index. Maxima of the ln(Fe/Ca) precession component are in phase with precession index maxima. The precession cycles in the ln(Fe/Ca) record appear particularly strong between ~0.9 and 0.6 Ma.
e), f) and g) present the same statistical analyses as in a), b) and c) respectively but for the PC1 SST record. For e) dashed white lines indicate the variability at the precession, obliquity and eccentricity periods. The three statistical analyses indicate significant variability at the 100 and 41 kyr periods but not significant power for the 400 kyr and 23 kyr (precession) periods.

Extended Data Figure 6: SST proxies reconstruction for core MD96-2048 over the last 2.14 Ma. a) Reconstruction of SST using two different methods: Mg/Ca reconstruction based on Caley et al.[15] data and new data. Mg/Ca ratios were converted into temperature values applying the equation established by Anand et al.[40]. Foraminifera transfer function reconstruction using the modern analogue technique. Error bars represent the error on the calibrations[40] (Extended data Fig. 7). b) Empirical Orthogonal Function (EOF) analysis[47] on the two SST records over the last 2.14 Ma. The Principal Component (PC1) contains 74 % of the total variance over the last 2.14 Ma. Correlation between SST proxies and PC1 over the last 2.14 Ma is R = 0.71.

Extended Data Figure 7: Foraminifera transfer function used for core MD96-2048. a) Location of the modern database composed of 367 core tops from the south Indian Ocean[45] with present day SST from WOA 2009[29]. b) Test for the modern database composed of 367 core tops from the south Indian Ocean[45] yielding to a precision of 0.8°C for the annual SST reconstructions. Modern hydrological parameters were obtained from the WOA (1998) database using the tool developed by Schäfer-Neth in the MARGO project (http://www.geo.uni-bremen.de/geomod/Sonst/Staff/csn/woasample.html).

Extended Data Table 1: Fossil finds, their location, and the associated ages. We consider the ages in bold as the best estimate. The different dating methods did not yield any agreement regarding the age of Kromdraai B and Sterkfontein Member 5 “Oldowan Infill”. Therefore, no estimate are highlighted in bold and the stratigraphic ranges are not showed in Fig. 3. We favor U-Pb dates and cosmogenic burial of quartz dates rather than biochronology or ESR (although dates are generally not inconsistent with the other methods)[145].*_P. robustus_ fossils were not found at GD1 and GD2 but nearby ex situ. Given the close age between GD1

and GD2 and the limited extent of outcrops, it was suggested that the ex situ hominin specimens from Gondolin should be dated around 1.78 Ma.

Extended Data Table 2: $\delta^{13}C$ enamel of hominin and contemporaneous herbivores and associated statistical parameters for different sites in the Limpopo catchment.

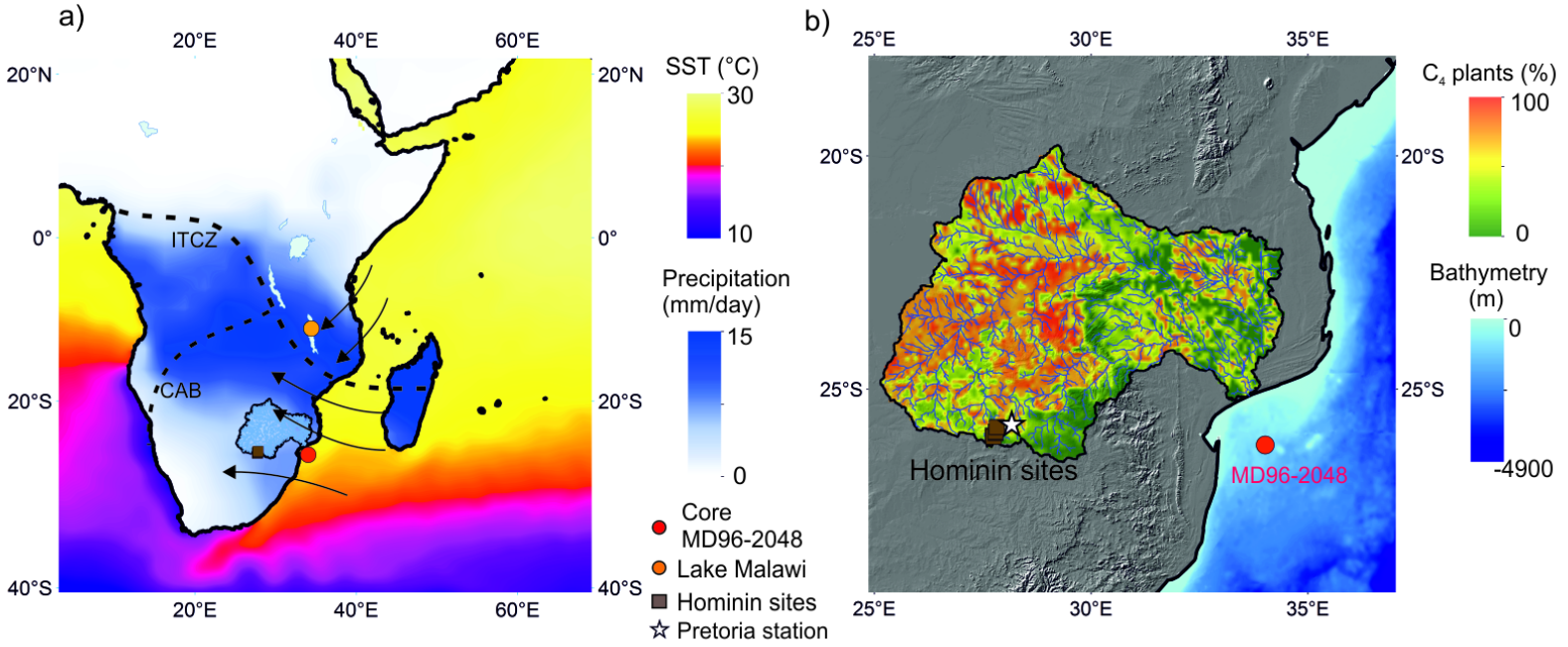
a)
20°E
40°E
60°E
20°N
0°
20°S
40°S
ITCZ
CAB
SST (°C)
30
10
Precipitation
(mm/day)
15
0
Core
MD96-2048
Lake Malawi
Hominin sites
Pretoria station
b)
25°E
30°E
35°E
20°S
25°S
Hominin sites
MD96-2048
C4 plants (%)
100
0
Bathymetry
(m)
0
-4900

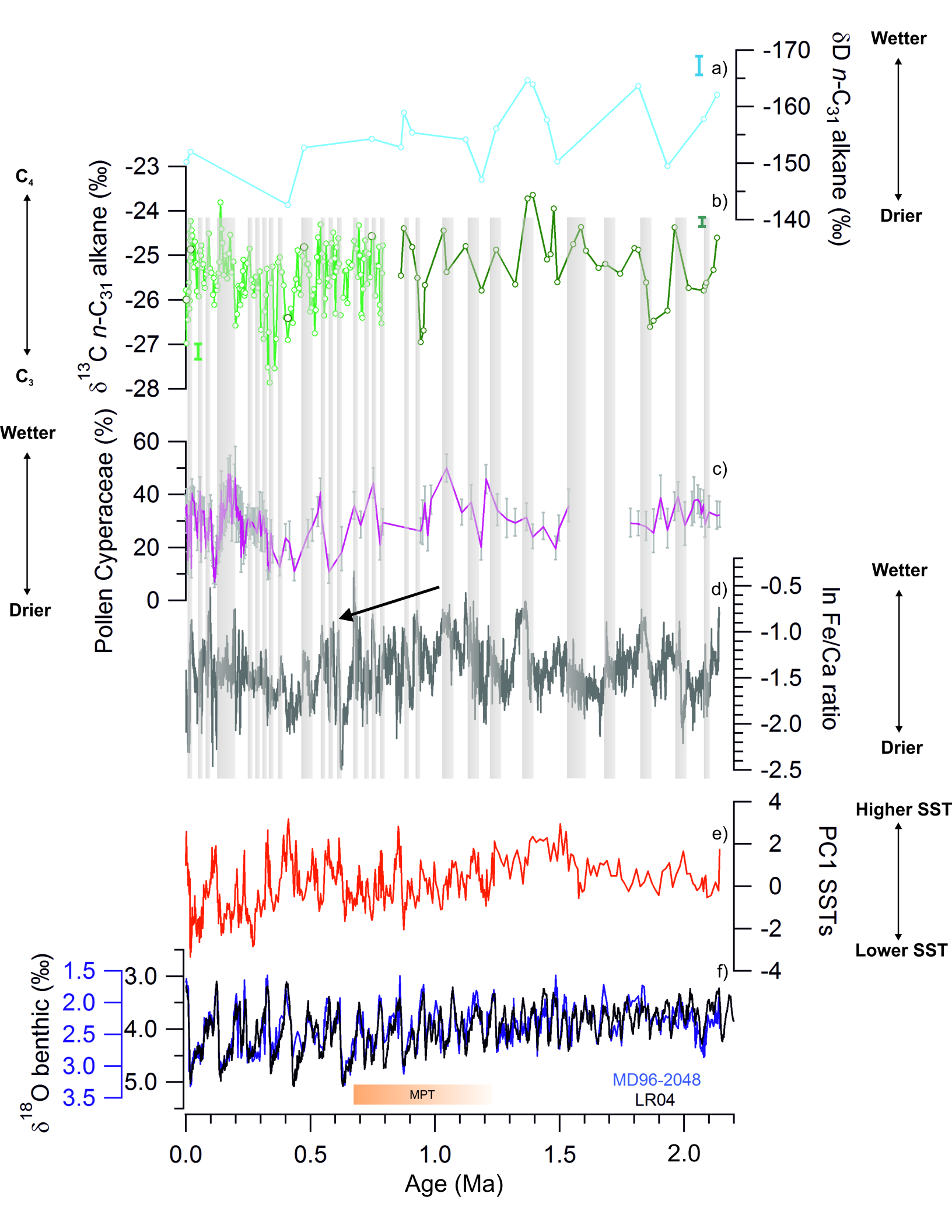
a)
b)
c)
d)
e)
f)
δD n-C31 alkane (‰)
-170
-160
-150
-140
Wetter
Drier
C4
C3
δ13C n-C31 alkane (‰)
-23
-24
-25
-26
-27
-28
Pollen Cyperaceae (%)
60
40
20
0
Wetter
Drier
ln Fe/Ca ratio
-0.5
-1.0
-1.5
-2.0
-2.5
Wetter
Drier
PC1 SSTs
4
2
0
-2
-4
Higher SST
Lower SST
δ18O benthic (‰)
1.5
2.0
2.5
3.0
3.5
3.0
4.0
5.0
MPT
MD96-2048
LR04
0.0
0.5
1.0
1.5
2.0
Age (Ma)

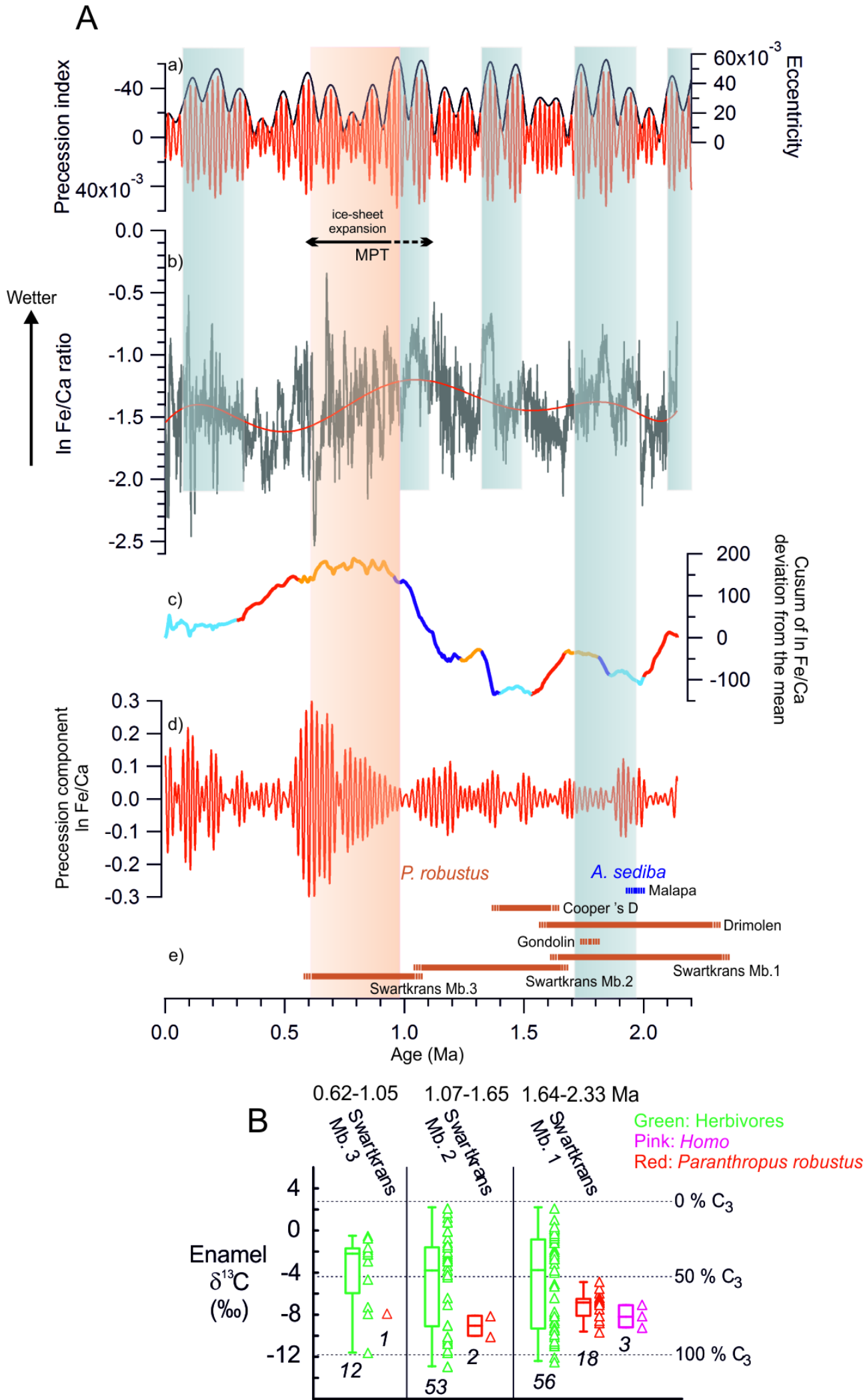
A
a)
Precession index
-40
0
40x10-3
60x10-3
40
20
0
Eccentricity
ice-sheet expansion
MPT
b)
Wetter
ln Fe/Ca ratio
0.0
-0.5
-1.0
-1.5
-2.0
-2.5
c)
200
100
0
-100
Cusum of ln Fe/Ca deviation from the mean
d)
Precession component ln Fe/Ca
0.3
0.2
0.1
0.0
-0.1
-0.2
-0.3
P. robustus
A. sediba
e)
Malapa
Cooper 's D
Drimolen
Gondolin
Swartkrans Mb.1
Swartkrans Mb.2
Swartkrans Mb.3
0.0
0.5
1.0
1.5
2.0
Age (Ma)
B
0.62-1.05
1.07-1.65
1.64-2.33 Ma
Swartkrans Mb. 3
Swartkrans Mb. 2
Swartkrans Mb. 1
Green: Herbivores
Pink: Homo
Red: Paranthropus robustus
Enamel δ13C (‰)
4
0
-4
-8
-12
0 % C3
50 % C3
100 % C3
12
1
53
2
56
18
3

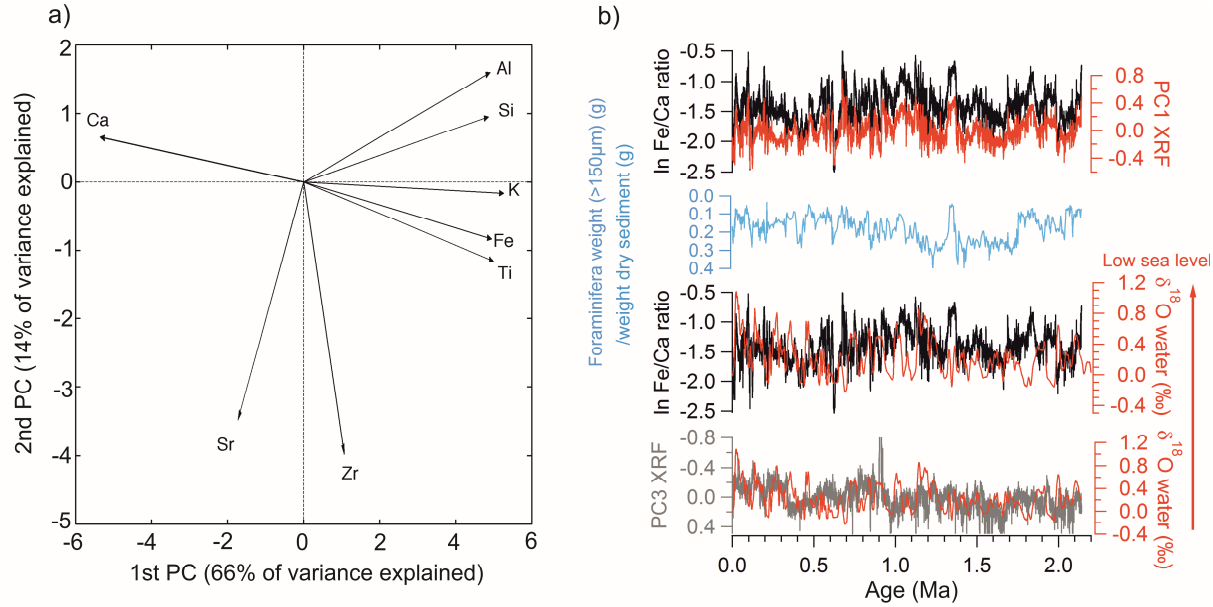
a)
2nd PC (14% of variance explained)
1st PC (66% of variance explained)
Al
Si
Ca
K
Fe
Ti
Sr
Zr
b)
ln Fe/Ca ratio
PC1 XRF
Foraminifera weight (>150µm) (g)
/weight dry sediment (g)
Low sea level
ln Fe/Ca ratio
δ18O water (‰)
PC3 XRF
δ18O water (‰)
Age (Ma)

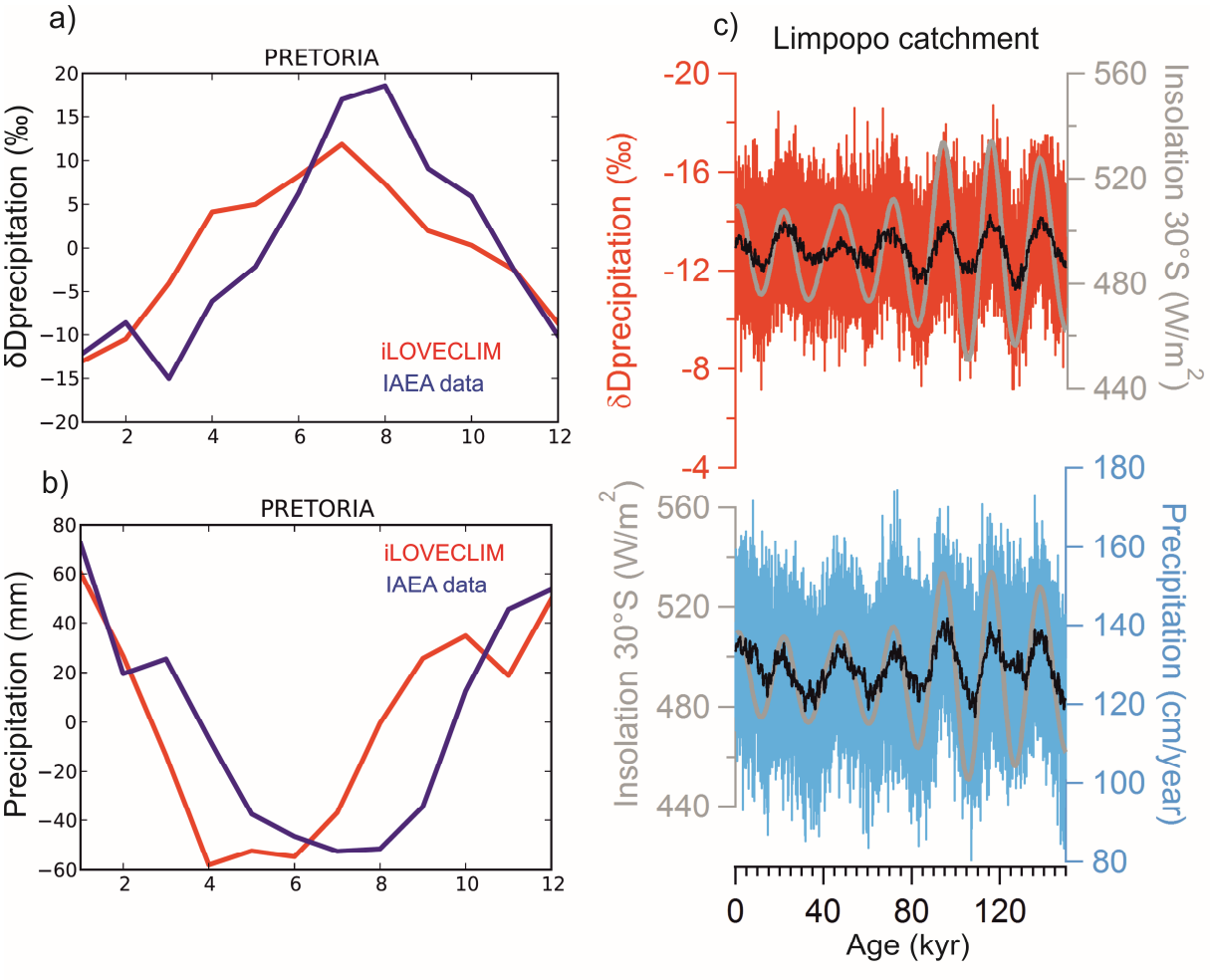
a)
PRETORIA
δDprecipitation (‰)
iLOVECLIM
IAEA data
b)
PRETORIA
Precipitation (mm)
iLOVECLIM
IAEA data
c)
Limpopo catchment
δDprecipitation (‰)
Insolation 30°S (W/m2)
Insolation 30°S (W/m2)
Precipitation (cm/year)
Age (kyr)

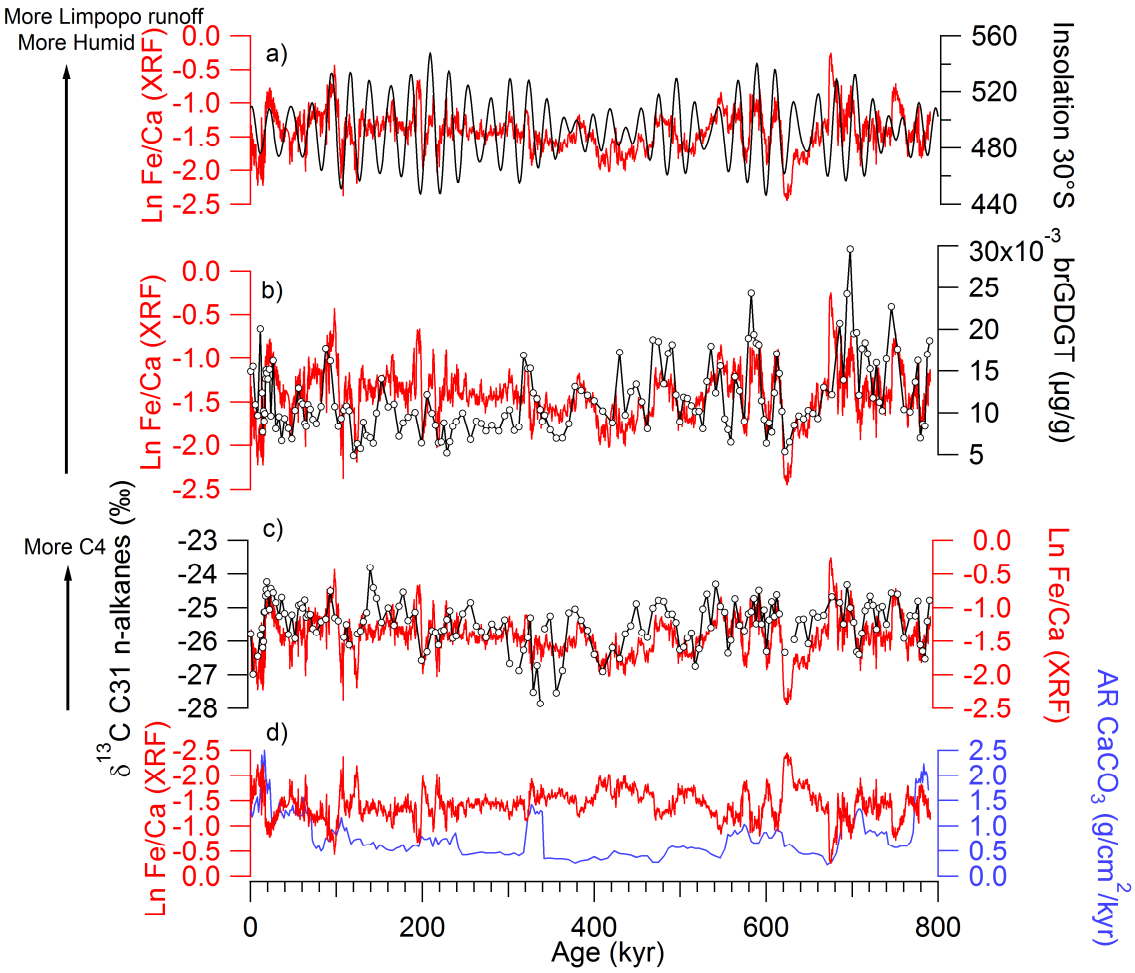
More Limpopo runoff
More Humid
a)
b)
c)
d)
Ln Fe/Ca (XRF)
Insolation 30°S
brGDGT (µg/g)
More C4
δ13C C31 n-alkanes (‰)
AR CaCO3 (g/cm2/kyr)
Age (kyr)
0
200
400
600
800

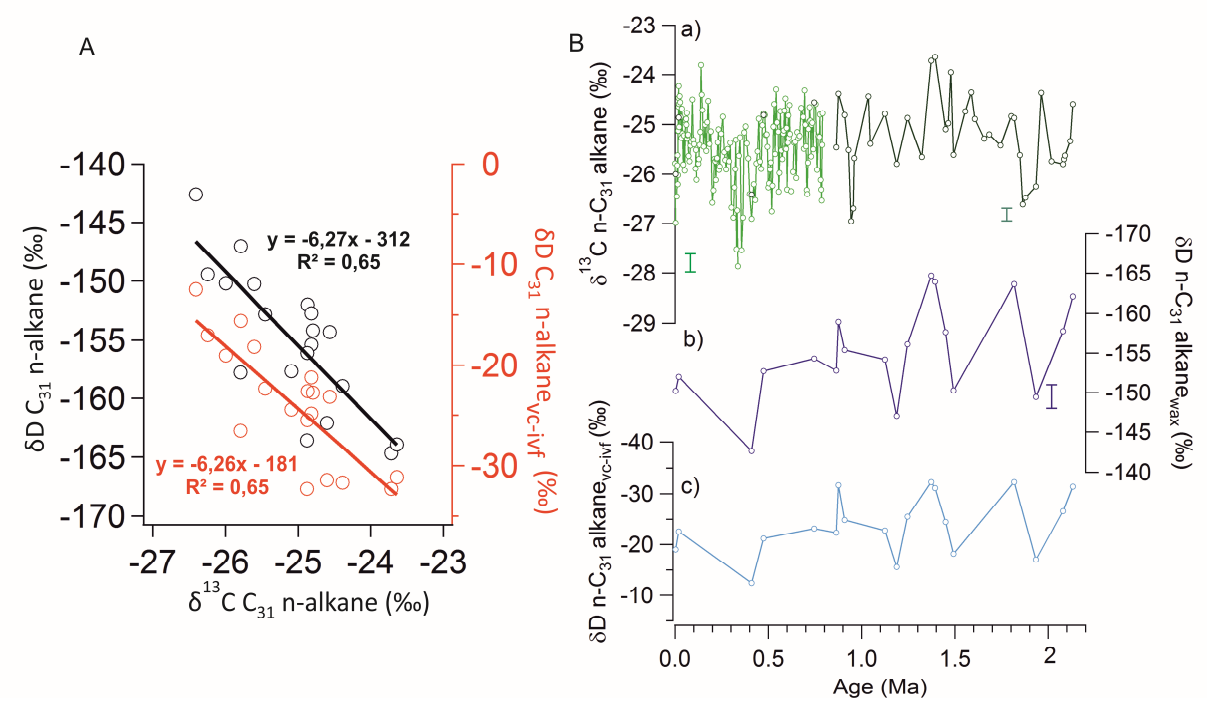
A
y = -6,27x - 312
R² = 0,65
y = -6,26x - 181
R² = 0,65
δD C31 n-alkane (‰)
δD C31 n-alkanevc-ivf (‰)
δ13C C31 n-alkane (‰)
B
a)
b)
c)
δ13C n-C31 alkane (‰)
δD n-C31 alkanewax (‰)
δD n-C31 alkanevc-ivf (‰)
Age (Ma)

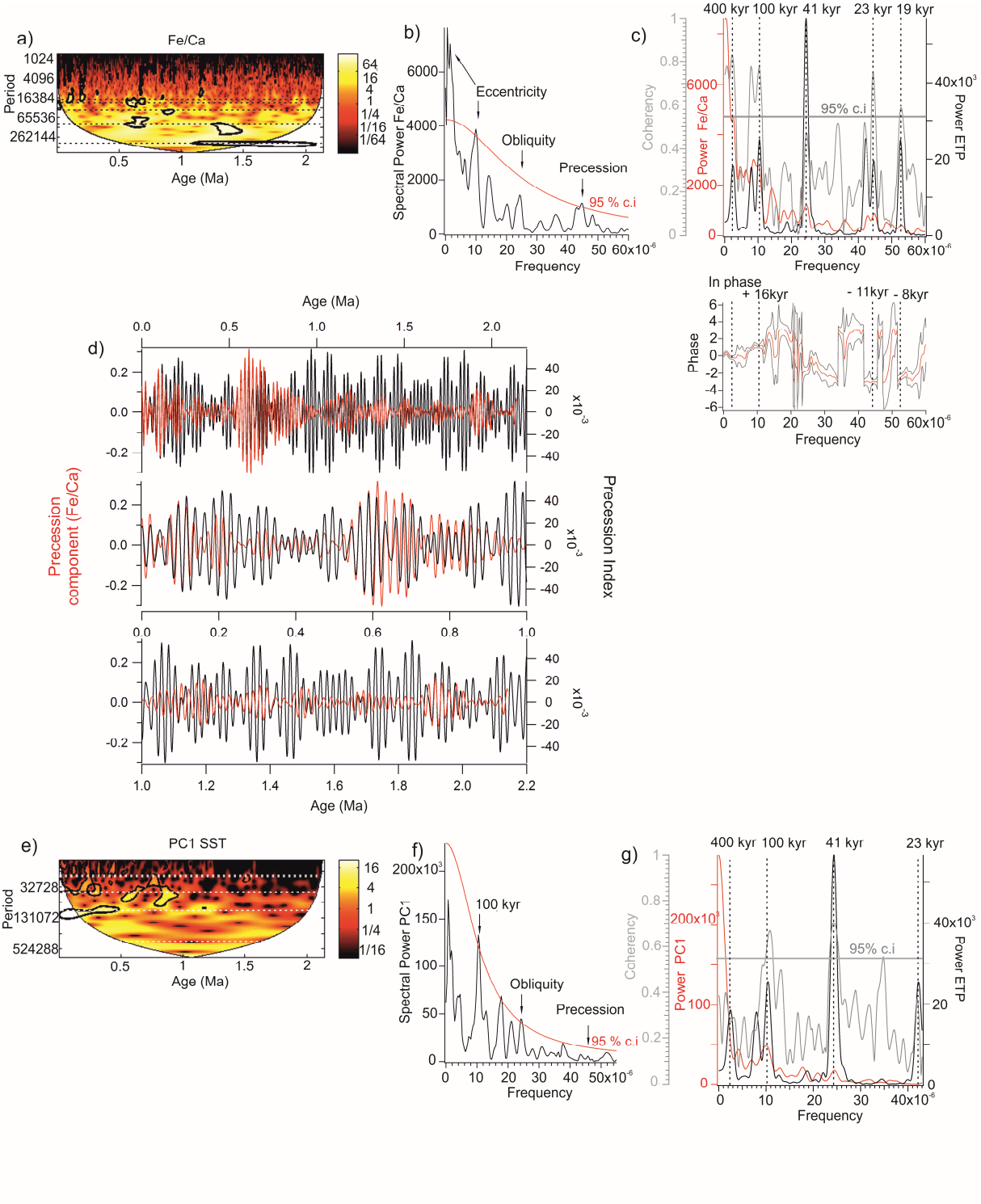
a)
Fe/Ca
Period
1024
4096
16384
65536
262144
0.5
1
1.5
2
Age (Ma)
64
16
4
1
1/4
1/16
1/64
b)
Spectral Power Fe/Ca
6000
4000
2000
0
Eccentricity
Obliquity
Precession
95 % c.i
0 10 20 30 40 50 60x10-6
Frequency
c)
400 kyr 100 kyr 41 kyr 23 kyr 19 kyr
Coherency
1
0.8
0.6
0.4
0.2
0
Power Fe/Ca
6000
2000
0
95% c.i
40x10³
20
0
Power ETP
0 10 20 30 40 50 60x10-6
Frequency
In phase
+ 16kyr
- 11kyr
- 8kyr
Phase
6
4
2
0
-2
-4
-6
0 10 20 30 40 50 60x10-6
Frequency
Age (Ma)
d)
0.0 0.5 1.0 1.5 2.0
0.2
0.0
-0.2
40
20
0
-20
-40
x10-3
Precession component (Fe/Ca)
Precession Index
0.0 0.2 0.4 0.6 0.8 1.0
1.0 1.2 1.4 1.6 1.8 2.0 2.2
Age (Ma)
e)
PC1 SST
Period
32728
131072
524288
0.5
1
1.5
2
Age (Ma)
16
4
1
1/4
1/16
f)
Spectral Power PC1
200x10³
150
100
50
0
100 kyr
Obliquity
Precession
95 % c.i
0 10 20 30 40 50x10-6
Frequency
g)
400 kyr 100 kyr 41 kyr 23 kyr
Coherency
1
0.8
0.6
0.4
0.2
0
Power PC1
200x10³
100
0
95% c.i
40x10³
20
0
Power ETP
0 10 20 30 40x10-6
Frequency

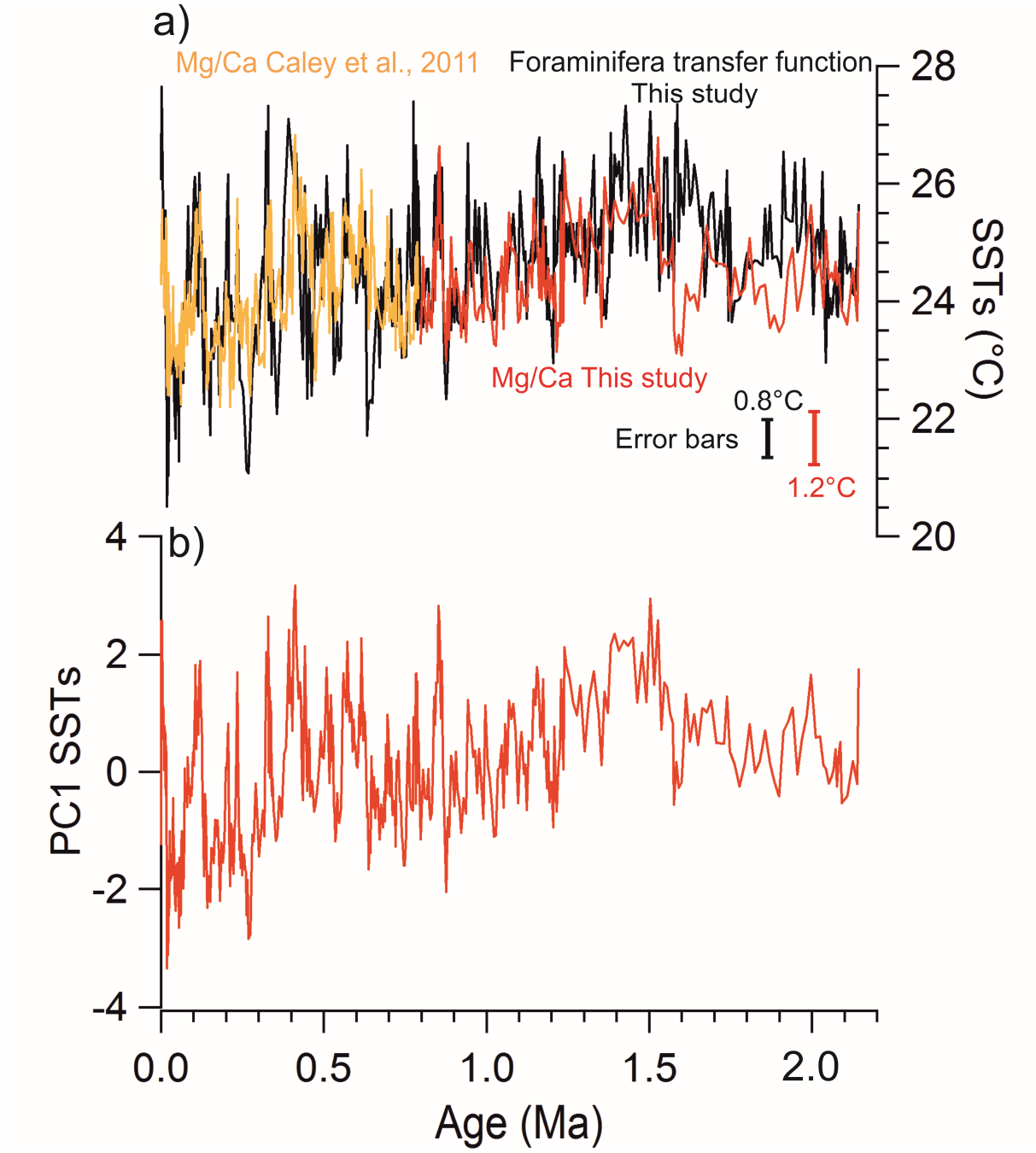
a)
Mg/Ca Caley et al., 2011
Foraminifera transfer function
This study
Mg/Ca This study
0.8°C
Error bars
1.2°C
SSTs (°C)
28
26
24
22
20
b)
PC1 SSTs
4
2
0
-2
-4
0.0
0.5
1.0
1.5
2.0
Age (Ma)

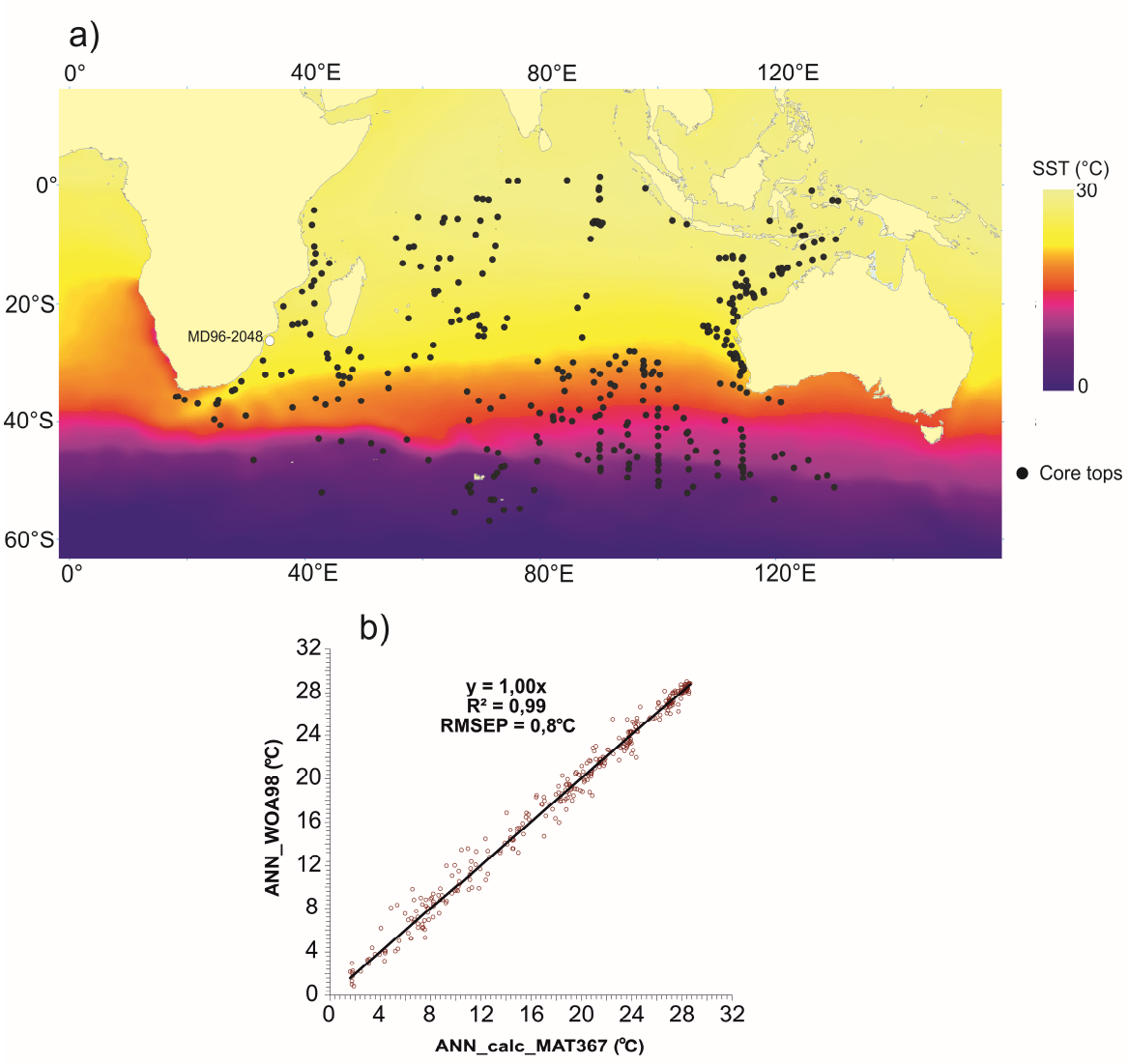
a)
0°
40°E
80°E
120°E
0°
20°S
40°S
60°S
MD96-2048
SST (°C)
30
0
Core tops
b)
y = 1,00x
R² = 0,99
RMSEP = 0,8°C
ANN_WOA98 (°C)
ANN_calc_MAT367 (°C)
0
4
8
12
16
20
24
28
32

Site/area	Taxon	Stratigraphic unit	Methods	References	Estimated age of fossils
Malapa	*Australopithecus sediba*		Biochronology	Dirks et al. (137)	From 1.95 Ma to 1.78 Ma
			U-Pb dating of flowstones: basal flowstone 1 at 2.026 ± 0.021 Ma; capping flowtone 2 at 2.048 ± 0.140 Ma	Pickering et al. (138)	From 2.188 Ma to 1.908 Ma
			Paleomagnetism : reversed polarity of flowstone 2, normal polarity of fossiliferous sediments	Pickering et al. (138)	Older than 1.95 Ma
			Synthesis of flowstone dating and paleomagnetism, 1.977 ± 0.002 Ma	Pickering et al. (138)	**From 1.979 to 1.975 Ma**
Cooper's D	*Paranthropus robustus*		Biochronology	Berger et al. (139)	From 1.9 Ma to 1.6 Ma
			U-Pb dating of flowstones: basal flowstone CDD1 at 1.526 ± 0.088 Ma; younger flowstone CDD3, intercalated within fossiliferous sequence, at ca. 1.4 Ma (unprecise dating from 1.617 Ma to 1.413 Ma)	de Ruiter et al. (140)	**From 1.615 Ma to ca. 1.4 Ma (upper facies A and C) and younger than 1.4 Ma (lower facies A and C)**
Drimolen	*P. robustus*	Main Quarry Site	Biochronology	Keyser et al. (141)	From 2.0 Ma to 1.5 Ma
			Biochronology	Adams et al. (142)	**From 2.3 Ma to 1.6 Ma**
Kromdraai B	*P. robustus*		Paleomagnetism of flowstone above Mb. 3, reverse polarity, older than normal Olduvai event (between 1.95 Ma and 1.78 Ma)	Thackeray et al. (143)	Older than 1. 95 Ma
			Alternative interpretation of paleomagnetic data from Thackeray et al. (2002)	Herries et al. (144); Herries & Adams (145)	From 1.78 Ma to 1.65 Ma
			Biochronology (including hominins) and paleomagnetism	Braga et al. (146)	Older than 2.18 Ma
Gondolin	*P. robustus*	GD2*	Biochronology and paleomagnetism (Olduvai normal polarity event of fossiliferous sediments)	Herries et al. (147)	**Slightly older than 1.78 Ma**
	P. robustus	GD1*	Biochronology and paleomagnetism (end of Olduvai normal polarity event in basal flowstone)	Adams et al. (148)	**Slightly younger than 1.78 Ma**
Sterkfontein	*P. robustus*	Mb. 5B "Oldowan infill"	Biochronology and lithic typology	Kuman & Clarke (106)	From 2.0 Ma to 1.7 Ma
		Mb. 5B "Oldowan infill"	ESR on bovid teeth (seven dates): 1.328 ± 0.087 Ma; 1.315 ± 0.295 Ma; 1.185 ± 0.96 Ma; 1.265 ± 0.125 Ma; 1.620 ± 0.626 Ma; 0.965 ± 0.147 Ma; 1.24 ± 0.28 Ma; weighed mean = 1.32 ± 0.08 Ma	Curnoe (149) reinterpreted in Herries & Shaw (150)	From 1.40 Ma to 1.24 Ma
		Mb. 5B "Oldowan infill"	Synthesis of ESR, U-Pb dating, paleomagnetism	Herries & Shaws (150)	From ca. 1.4 Ma to 1.2 Ma
		Mb. 5B "Oldowan infill"	ESR on teeth from 0.965 ± 0.147 Ma to 1.328 ± 0.087 Ma ; weighted mean LU-ESR (excluding one tooth with large internal errors) = 1.223 ± 0.155 Ma	Curnoe (149) reinterpreted in Herries et al. (144)	from 1.415 Ma to 1.241 Ma (maximal); 1.112 Ma to 0.818 Ma (minimal); from 1.378 Ma to 1.223 (weighed mean)
		Mb. 5B "Oldowan infill"	Cosmogenic burial ($^{26}Al/^{10}Be$) dating of a quartz manuport 2.18 ± 0.21 Ma	Granger et al. (151)	From 2.39 Ma to 1.97 Ma
		Mb. 5B "Oldowan infill"	Synthesis of paleomagnetism, U-Pb dating, and ESR	Herries & Adams (145)	From 1.8 Ma to 1.5 Ma
		Mb. 5B "Oldowan infill"	Synthesis of biochronology and ESR	Herries et al. (144)	From 1.38 Ma to 1.07 Ma
Swartkrans	*P. robustus*	Mb. 1	Cosmogenic burial ($^{26}Al/^{10}Be$) dating on quartz 2.19 ± 0.08 Ma	Gibbon et al. (152)	From 2.27 Ma to 2.11 Ma
		Mb. 1	Cosmogenic burial ($^{26}Al/^{10}Be$) dating on quartz 1.80 ± 0.09 Ma	Gibbon et al. (152)	From 1.89 Ma to 1.71 Ma
		Mb. 1 Hanging Remnant	Synthesis of U-Pb dating and ESR	Herries & Adams (145)	From 2.0 Ma to 1.8 Ma
		Mb. 1 Hanging Remnant	ESR 2.02 ± 0.36 Ma; 2.07 ± 0.37 Ma; 1.68 ± 0.28 Ma; weighed mean = 1.96 Ma-1.70 Ma	Curnoe et al. (153) reinterpreted in Herries & Adams (145)	From 1.96 Ma to 1.70 Ma
		Mb. 1 Hanging Remnant	ESR LU 1.39 ± 0.18 Ma	Herries et al. (144)	From 1.57 Ma to 1.21 Ma
		Mb. 1 Hanging Remnant	ESR LU 1.92 ± 0.34 Ma	Herries et al. (144)	From 2.26 Ma to 1.58 Ma
		Mb. 1 Hanging Remnant	ESR LU 1.21 ± 0.22 Ma	Herries et al. (144)	From 1.43 Ma to 0.99 Ma
		Mb. 1 Lower Bank	U-Pb dating	Pickering et al. (154)	From 2.3 to 1.6 Ma
		Mb. 1	U-Pb dating on tooth 1.83 ± 1.38 Ma	Balter et al. (155) Vrba (156, 157);	From 3.21 to 0.45 Ma
		Mb. 1	Biochronology	Churcher & Watson (158)	ca. 1.7 Ma
		Mb. 1	U-Pb dating of basal flowstone 2.249 ± 0.077 Ma; top flowstone 1.706 ± 0.069 Ma ; closer to 2.0 Ma-1.8 Ma	Pickering et al. (154)	**Maximal range from 2.326 Ma to 1.637 Ma; minimal range from 2.172 Ma to 1.775 Ma**
Swartkrans	*P. robustus*	Mb. 2	U-Pb dating on tooth 1.36 ± 0.29 Ma	Balter et al. (155) Vrba (156, 157);	**From 1.65 Ma to 1.07 Ma**
		Mb. 2	Biochronology	Churcher & Watson (158)	ca. 1.5 Ma
		Mb. 2	Relative position to Mb. 1 dated by U-Pb	Pickering et al. (154)	Younger than ca. 1.7 Ma
Swartkrans	*P. robustus*	Mb. 3	Synthesis of U-Pb and ESR dating	Herries & Adams (145)	From 1.3 Ma to 0.6 Ma
		Mb. 3	Cosmogenic burial on quartz 0.96 ± 0.09 Ma	Gibbon et al. (152)	**From 1.05 Ma to 0.87 Ma**
		Mb. 3	ESR 0.65 ± 0.15 Ma	Cited in Herries and Adams (145)	From 0.8 Ma to 0.5 Ma
		Mb. 3	ESR 1.25 ± 0.09 Ma	Cited in Herries and Adams (145)	From 1.34 Ma to 1.16 Ma
		Mb. 3	U-Pb dating on tooth 0.83 ± 0.21 Ma	Balter et al. (155) Vrba (156, 157);	**From 1.04 Ma to 0.62 Ma**
		Mb. 3	Biochronology	Churcher & Watson (158)	ca. 1.0 Ma
		Mb. 3	ESR LU on two bovid teeth (four dates): 0.71 ± 0.90 Ma and 0.80 ± 015 Ma; 0.65 ± 0.15 Ma and 0.70 ± 0.11 Ma; mean = 0.72 ± 0.13 Ma	Blackwell (159)	From 0. 85 Ma to 0.59 Ma
		Mb. 3	Synthesis of biochronology and U-Pb	Herries et al. (144)	**From 1.04 Ma to 0.62 Ma**

Group	n	$\delta^{13}C$ (‰) mean	median	mode(s) (2 ‰ interval)	SD	min	max	range	References
Cooper' D herbivores	45	-5,0	-4,7	int. 1: -12 to -10 ‰ ; int. 2: -2 to 0 ‰	3,9	-11,5	2,5	14,0	Steininger (101)
Gondolin GD2 herbivores	21	-2,9	1,0	int. 1: -10 to -8 ‰ ; int. 2: 0 to 2 ‰	5,3	-11,1	3,5	14,6	Adams (102)
Swartkrans Mb. 1 herbivores	56	-4,8	-3,8	int. 1: -10 to -8 ‰ ; int. 2: -4 to 0 ‰	4,2	-12,4	2,2	14,6	Lee-Thorp et al. (99); Sponheimer et al. (83); Steininger (160)
Swartkrans Mb. 1 *Paranthropus*	18	-7,2	-6,9	int.: -8 to -6 ‰	1,2	-9,6	-4,9	4,7	Lee-Thorp et al. (99); Sponheimer et al. (84, 83)
Swartkrans Mb. 1 *Homo*	3	-8,2	-8,2	int.: -10 to -8 ‰	0,9	-9,2	-7,1	2,1	Lee-Thorp et al. (100)
Swartkrans Mb. 2 herbivores	53	-4,8	-3,8	int. 1: -12 to -10 ‰ ; int. 2: -4 to -2 ‰	4,4	-12,9	2,2	15,1	Lee-Thorp et al. (99, 100); Steininger (160)
Swartkrans Mb. 2 *Paranthropus*	2	-9,1	-9,1			-10,0	-8,1	1,9	Lee-Thorp et al. (99)
Swartkrans Mb. 3 herbivores	12	-3,8	-2,2	int.: -4 to 0 ‰	3,3	-11,6	-0,5	11,1	Steininger (160)
Swartkrans Mb. 3 *Paranthropus*	1	-7,9	-7,9			-7,9	-7,9		Lee-Thorp et al. (99)